https://doi.org/10.5194/egusphere-2026-948
Preprint. Discussion started: 21 April 2026

New operational perspective to identify aerosol in real-time with a pioneering algorithm (CONIOPOL) based on single wavelength polarization lidar (CL61).

Quentin Laffineur[1], Alexander Mangold[1], Andy W. Delcloo[1,2]

[1]Royal Meteorological Institute of Belgium, Observations Department, Atmospheric Composition, Measurement and Modelling group, ACM², Uccle, 1180, Belgium
[2]Ghent University, Department of Physics and Astronomy, Ghent, 9000, Belgium

Correspondence to: Quentin Laffineur (Quentin.laffineur@meteo.be)

Abstract

Air quality monitoring and climate studies require continuous, vertically resolved observations to characterize aerosols and their impact on radiation, cloud microphysics, and atmospheric composition. In this study, we present CONIOPOL (CONIOlogy + POLarization), an automated depolarization-based classification algorithm developed with the polarized Automatic Lidar Ceilometer (ALC), CL61 (Vaisala Oyi, FIN) installed at Uccle, Belgium. The algorithm combines linear depolarization ratio (LDR), attenuated backscatter, and cloud-base height retrievals to distinguish between aerosols, clouds, and precipitation, and to further classify aerosol subtypes.

One full year (February 2024–January 2025) of observations was analyzed to retrieve and evaluate the seasonal and vertical distributions of major aerosol categories, with results compared against Copernicus Atmosphere Monitoring Service (CAMS) model forecast outputs. The CONIOPOL algorithm successfully identified different types of aerosol —including dust, smoke, hygroscopic, and mixed aerosols—demonstrating strong temporal and vertical coherence with CAMS simulations. In particular, dust and smoke plumes detected above 1000 m showed a good agreement with it.

Despite its spectral limitations, the single-wavelength lidar provides continuous, high-resolution, and climatologically consistent aerosol classification, offering valuable insights into the seasonal evolution of aerosol types over mid-latitude Europe. These findings underscore the potential of depolarization-capable ALCs for long-term aerosol and air quality climatology, bridging temporal gaps between satellite, in situ, and multi-wavelength lidar observations.

1 Introduction

Aerosols and clouds are key components of the Earth's atmosphere, exerting a major influence on climate, air quality, and weather systems through their interactions with radiation and cloud microphysics (Illingworth et al., 2015; IPCC, 2023). They modulate the Earth's radiative balance by scattering and absorbing solar and terrestrial radiation and by acting as cloud condensation and ice-nucleating particles. Understanding their vertical distribution, composition, and evolution is therefore essential for constraining radiative forcing estimates and improving both weather and climate models.

In recent years, Europe has experienced an increased recurrence of transcontinental aerosol events, notably Saharan dust intrusions carried thousands of kilometers northward (Cuevas-Agulló et al., 2024; Monteiro et al., 2022; Vogel et al., 2025), and long-range smoke plumes from intense wildfires in North America, particularly Canada (Baars et al., 2021; Hu et al., 2019; Markowicz et al., 2016; Masoom et al., 2025; Sicard et al., 2019). These episodes can substantially modify the atmospheric radiative budget, degrade air quality, and influence cloud properties far from their source regions. Characterizing and monitoring such events require continuous, vertically resolved observations capable of discriminating between aerosol types and quantifying their optical and microphysical properties.

Aerosol vertical profiles can be obtained using a range of observational methods. In situ measurements from aircraft (e.g. Jurányi et al., 2025), balloons-borne (e.g. Ravi Kiran et al., 2022), hot-air balloons (e.g. Petäjä et al., 2012), zeppelins (e.g. Tillmann et al., 2022), towers (e.g. Franco et al., 2024), or unmanned aerial vehicles (e.g. Brus et al., 2021) provide detailed chemical and microphysical characterizations but are limited in temporal and spatial coverage. In contrast, active remote sensing with lidar systems enables continuous retrievals of aerosol optical properties, allowing high-resolution monitoring of the vertical structure of aerosols and clouds.

Depolarization is one of the most powerful lidar observables for differentiating aerosol and cloud types. It arises from the modification of the polarization state of backscattered light by non-spherical particles such as mineral dust, volcanic ash, or ice crystals (Freudenthaler et al., 2009). Spherical particles, in contrast, preserve the incident polarization, producing low depolarization ratios. The linear depolarization ratio (LDR) thus provides a robust means of classifying atmospheric particles into depolarizing (e.g., dust, ice) and non-depolarizing (e.g., smoke, sulfate) types. Depolarization measurements also enable cloud-phase identification, distinguishing liquid-phase clouds composed of nearly spherical droplets from ice-phase clouds containing non-spherical crystals (Lewis et al., 2020; Neely et al., 2013).

Satellite observations based on depolarization are essential in this context, as they provide global, continuous, and synoptic coverage, capturing long-range transport events that ground-based instruments alone cannot resolve. Instruments such as CALIOP (Cloud-Aerosol Lidar with Orthogonal Polarization, Winker et al., 2009) aboard CALIPSO measure LDR in the vertical column, allowing discrimination between spherical and non-spherical particles. Similarly, depolarization-capable spaceborne lidars such as ATLID onboard ESA's EarthCARE mission (Illingworth et al., 2015; Wehr et al., 2023) exploit LDR to identify aerosol types and cloud phases with high vertical resolution. By providing repeated, large-scale measurements, satellite depolarization observations are crucial for detecting and tracking transcontinental aerosol transport events—such as Saharan dust or North American smoke plumes—and for validating global and regional aerosol transport models.

Airborne lidar systems further complement spaceborne observations by offering flexible, high-resolution measurements over targeted regions. Instruments such as NASA's High Spectral Resolution Lidar (HSRL; Burton et al., 2018; Hair et al., 2008) and the French LNG lidar aboard the SAFIRE Falcon 20 (Chazette et al., 2019) can accurately profile aerosol and cloud optical properties with fine vertical and horizontal resolution, bridging the scale gap between satellite and ground-based measurements.

Complementary to these spaceborne and airborne systems, ground-based lidar networks, including multi-wavelength lidar and single-wavelength ALC systems, provide continuous, high-temporal-resolution observations of the vertical structure of aerosols and clouds (Illingworth et al., 2019) usually covering the whole troposphere. Multi-wavelength lidars represent the most advanced class of ground-based systems, as they combine measurements at several laser wavelengths and polarization states. This synergy allows for a more comprehensive retrieval of aerosol optical and microphysical properties, including particle size distribution, refractive index, and complex mixtures (Müller et al., 2007). In contrast, single-wavelength systems such as ALCs offer robust and continuous profiling but remain limited in their capability to characterize particle size and composition (Madonna et al., 2015, 2018; Wiegner et al., 2014).

Recent technological developments have led to the commercial availability of compact ALCs equipped with depolarization channels, enabling unattended, routine monitoring of particle shape and cloud phase at a fraction of the cost of multi-wavelength lidars. Among commercially available instruments, only two currently integrate depolarization capability with single wavelength: the Vaisala CL61 (ALC) and the Halo Photonics StreamLine Doppler wind lidar. Both have been validated in numerous studies demonstrating their accuracy and suitability for operational applications. The Vaisala CL61 has been employed for a wide range of aerosol and cloud studies (Bedoya-Velásquez et al., 2022; Chen et al., 2025; Filioglou et al., 2023, 2025; Inoue et al., 2025; Inoue and Sato, 2023; Karle et al., 2025; Looschelders et al., 2025; Tukiainen et al., 2025), while the Halo Photonics StreamLine has been used to investigate aerosol–cloud interactions and to validate depolarization retrievals (Bohlmann et al., 2021; Le et al., 2024; Vakkari et al., 2021).

Recent studies have developed increasingly sophisticated frameworks for aerosol classification based on the linear depolarization ratio (LDR) and complementary optical parameters. Multi-wavelength lidar observations have shown that combining LDR, backscatter, and lidar ratio enables reliable discrimination among major aerosol types, including dust, smoke, and marine particles (Baars et al., 2017; Burton et al., 2012; Groß et al., 2013). However, similar classifications can also be achieved with single-wavelength systems when rigorously calibrated against reference instruments, as demonstrated by Papetta et al. (2024). This highlights that, while multi-wavelength lidars provide more detailed insights into aerosol microphysics, properly calibrated single-wavelength systems can still deliver valuable classification capabilities.

Depolarization-based aerosol classification typically follows a stepwise, decision-tree approach. Lidar signals are first calibrated to retrieve LDR and backscatter profiles, after which LDR thresholds distinguish spherical from non-spherical particles. Auxiliary parameters such as lidar ratio, backscatter coefficient, and Ångström exponent further refine the classification, including the identification of mixed or layered aerosols. Additional temporal and vertical averaging, along with quality screening, helps reduce uncertainties related to noise and layer overlap. This modular framework allows ground-based depolarization lidars to produce continuous, high-resolution aerosol and cloud typing for both climatological and operational applications.

In parallel, machine learning (ML) methods have become powerful tools for lidar-based aerosol classification. Supervised algorithms such as Random Forests and Support Vector Machines trained on labeled datasets can capture nonlinear relationships among lidar-derived variables, improving classification accuracy under diverse conditions (del Águila et al., 2025; Farhani et al., 2021; Nicolae et al., 2018). More recently, deep learning (DL) architectures, particularly Convolutional Neural Networks (CNNs), have shown strong potential for identifying complex aerosol features directly from vertical profiles. CNNs can extract spatial patterns within lidar signals, enabling finer discrimination of mixed or overlapping aerosol layers (Lolli, 2023). These advances indicate a growing trend toward hybrid frameworks that combine physical constraints with ML-based feature extraction, aiming to leverage the strengths of both physics-driven and data-driven approaches for improved aerosol and cloud classification.

However, aerosol classification using single-wavelength depolarization measurements remains particularly challenging, as it requires careful calibration and robust algorithms to separate aerosol types and cloud phases under varying atmospheric conditions. CONIOPOL algorithm was developed at Royal Meteorological Institute of Belgium to automatically classify atmospheric targets detected by the CL61 at the Uccle site in Brussels, Belgium. The algorithm combines depolarization, backscatter, and cloud base height data to distinguish between aerosols, clouds, and precipitation and to further categorize aerosol types. By integrating filtering, smoothing, threshold-based classification, and clustering methods, CONIOPOL enables continuous, high-resolution monitoring of aerosol–cloud interactions and their seasonal variability.

The present study has three main objectives:

- To describe and implement the CONIOPOL algorithm for depolarization-based classification using the Vaisala CL61.
- To evaluate the performance and stability of the instrument calibration and algorithm thresholds at the Uccle site over an annual cycle.
- To validate aerosol classifications against model outputs from CAMS and to analyze seasonal and vertical distributions of major aerosol categories.

Uccle provides an ideal testbed for this study, owing to its long-term atmospheric observation record and its location in a temperate oceanic environment, influenced by both natural and anthropogenic aerosol sources. The synergy between continuous lidar observations and model simulations offers a pathway to enhance the operational use of ALC depolarization data for aerosol monitoring and to support the development of automated classification systems within European observation networks.

2 Site description

The Uccle site is located in the southern part of Brussels (50.8° N, 4.35° E) in Belgium at approximately 100 m above sea level. Established in 1886, it is one of the longest-running atmospheric monitoring stations in Europe and is member of many international networks such as the World Meteorological Organization's Global Atmosphere Watch (GAW), the Network for the Detection of Atmospheric Composition Change (NDACC), and in near future in the Aerosols, Clouds, and Trace Gases Research Infrastructure (ACTRIS). The site is situated within a suburban environment, including residential neighborhoods, parks, and green spaces, minimizing local pollution influences and ensuring that measurements are representative of regional atmospheric conditions.

Uccle experiences a temperate oceanic climate (Köppen classification: Cfb), prevailing westerly winds associated with the North Atlantic strongly favor the transport of aerosols from both regional and long-range sources. Westerly and southwesterly winds can carry mineral dust from the Sahara and southern Europe, sea salt from the North Sea, smoke from wildfires in southern Europe, or even Canada during extreme wildfire seasons, depending on synoptic conditions. Local and regional anthropogenic aerosols, including urban and industrial emissions, also contribute to the observed aerosol load, while natural sources such as biogenic aerosols play an additional role (Flemish Environment Agency, 2020; IRCELINE, 2023). These include primary biological particles (e.g., pollen, spores) as well as secondary organic aerosols formed from the oxidation of biogenic volatile organic compounds (BVOCs), particularly during the growing season. Seasonal variations in wind patterns, precipitation, and boundary-layer dynamics further control aerosol dispersion, mixing, and removal.

3 Vaisala CL61 Lidar Ceilometer

At Uccle, a single ALC (CL61, Vaisala Oyi, FIN) is installed. This instrument is designed for atmospheric profiling, providing advanced capabilities for cloud and aerosol detection (Roininen et al., 2025). Using a 910.55 nm InGaAs diode laser, the CL61 measures attenuated volume backscatter profiles with a vertical resolution of 4.8 m over a range from 0 to 15.4 km. A key feature distinguishing the CL61 from other ALC is its depolarization measurement capability, which enables the differentiation between solid, liquid, and mixed-phase cloud and precipitation particles. The degree of depolarization is influenced by both aerosols and air molecules and is expressed as the volume linear depolarization ratio (LDR), defined as the ratio of the cross-polarized (XPOL) to the parallel-polarized (PPOL) signal components. The CL61 alternates acquisition of XPOL and PPOL signals with an integration time of 0.2 s for each, and complete profiles are averaged over 5 s prior to analysis. The minimum averaging interval is 5 s for attenuated backscatter and 10 s for depolarization. In this study, for both a 30 s averaging interval is applied. This configuration enables detailed vertical profiling of the atmosphere, including the detection of cloud base heights (determined internally at a 5 s resolution, independent of user-defined averaging, based on data collected during the last 30 minutes), aerosol layers, and boundary layer structures. The manufacturer provides an instrument-specific overlap function, expressed as a percentage from 0 to 100%, which characterizes the region of incomplete optical overlap, also known as the blind zone. Wagner et al. (2024) recommend discarding observations in the blind zone, which they

https://doi.org/10.5194/egusphere-2026-948
Preprint. Discussion started: 21 April 2026

define as being from the height the overlap function reaches 3% down to the sensor. For the CL61 employed in this study, this height corresponds to 33.6 m, and therefore only data above this threshold are considered here.

The instrument operates autonomously under all weather conditions and requires only minimal maintenance, primarily the regular cleaning of the optical window, which is essential for preserving data quality. Measurement data and internal monitoring parameters are provided every 5 minutes in NetCDF format, ensuring interoperability with a wide range of reading tools. In this study, the measurement period considered spans from 13 February 2024 (instrument start-up) to 30 January 2025.

4 Algorithm design

The CONIOPOL algorithm uses range, attenuated backscatter signal, LDR, and CL61 cloud base detection to classify aerosol types, cloud phases, and precipitation types. Figure 1 presents the decision tree employed to determine this classification. Before initiating the classification at each range, CONIOPOL assesses whether clouds are detected and whether they are precipitating.

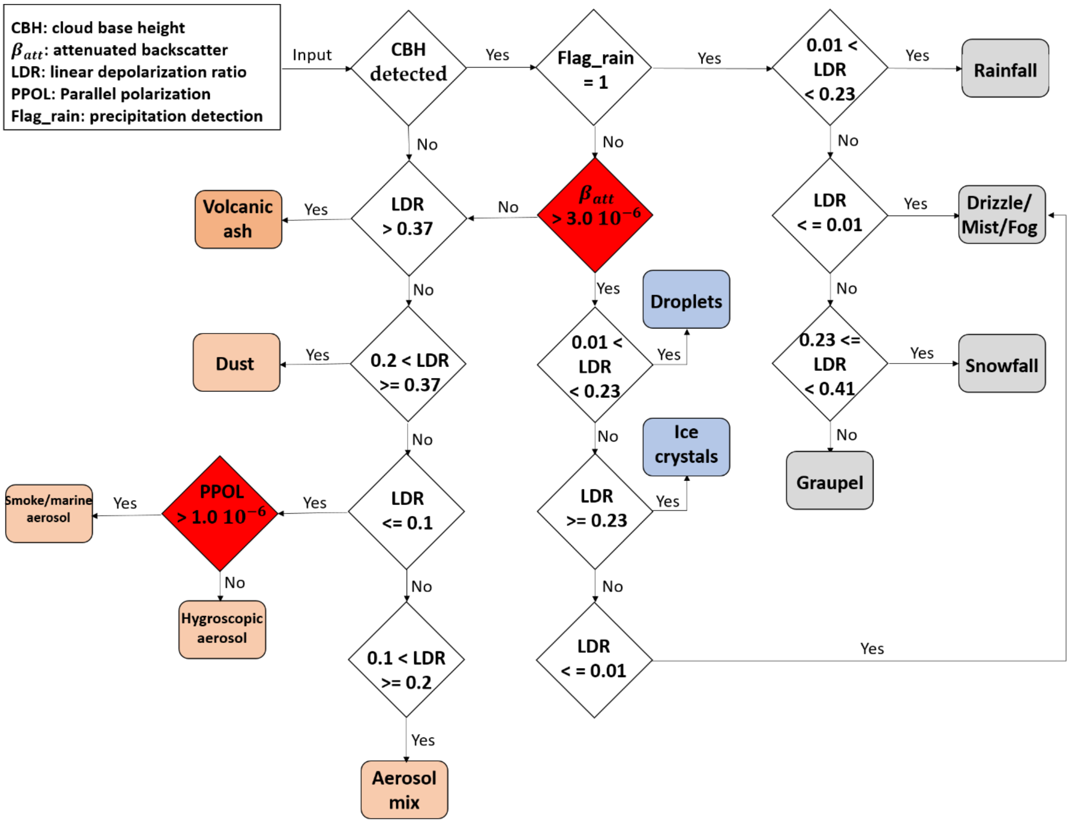

Figure 1: Decision tree for aerosol and cloud phase and precipitations classification applied in CONIOPOL. The flowchart illustrates the sequence of conditions used to discriminate the different target types based on lidar measurements (cloud base height, attenuated backscatter, LDR, PPOL).

4.1 Calibration

Accurate calibration of both backscatter profiles and depolarization is essential for the reliable performance of CONIOPOL in automatic target classification. The attenuated backscatter data provided by the CL61 are calibrated in manufactory using the cloud calibration method proposed by O'Connor et al., (2004), which relies on the well-characterized and stable optical properties of liquid water clouds. While the calibration constant can be updated, its stability should be verified through monthly monitoring to identify potential drifts from the factory setting and to ensure the long-term consistency of the backscatter measurements. In our case, the CL61 calibration remained stable throughout the analysis period.

Unlike more advanced lidars, the CL61 does not incorporate an internal calibrator for the depolarization channel, nor does it allow the user to modify the optical path to include one or to assess the depolarization effect of individual components. In the CL61, depolarization is measured using two filters positioned in front of a single avalanche photodiode detector on the coaxial optical path. Since the same receiver module is used for both PPOL and XPOL signals, no receiver sensitivity calibration is required.

Although the polarizer performance in this configuration is expected to remain stable, following the recommendations and methodology of Vakkari et al. (2021) for the Halo StreamLine lidar, we advise monitoring its performance monthly at the base of liquid water clouds. While spherical droplets do not inherently polarize the backscattered signal, the measured depolarization ratio is not exactly zero due to the non-simultaneous acquisition of PPOL and XPOL signals. This ratio exhibits a slight deviation from zero, reflecting temporal variations in the physical properties of the target between the two measurements. Moreover, multiple scattering within the cloud also contributes to an increase in the depolarization signal (Hu et al., 2006; Liou and Schotland, 1971). To minimize this impact on the ratio, only the first measurement points at the cloud base are used for calibration monitoring.

In Fig. 2, the LDR at the base of liquid clouds for each month exhibits no significant drift, with median values generally ranging from 0.01 to 0.02, in agreement with the values of Vakkari et al. (2021) and Le et al. (2024). The observed variability can be attributed to non-simultaneous signal acquisition and multiple scattering effects, as previously discussed, as well as to the occurrence of drizzle near the cloud base, although such events were filtered out during the analysis using the peak sharpness filter proposed by Hopkin et al. (2019). During the coldest months, some variability may also arise from mixed-phase clouds that were mistakenly considered as liquid-only (Le et al., 2024), which may partly explain the larger spread observed in November.

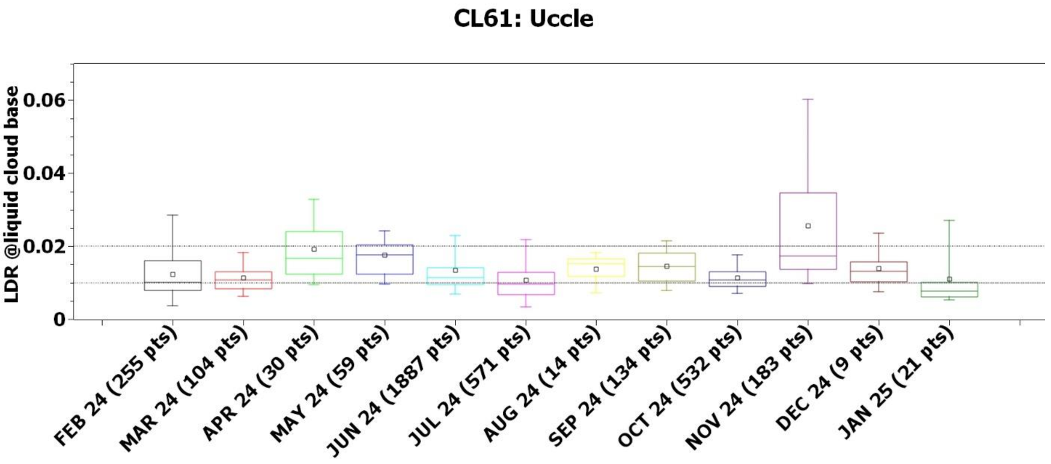

Figure 2: Boxplots of the linear depolarization ratio (LDR) recorded at the cloud base for each month after data filtering. The horizontal line within each box indicates the median, the square marker denotes the mean, the lower and upper bounds of each box correspond to the 25th and 75th percentiles, and the whiskers extend to the 5th and 95th percentiles.

4.2 SNR filtering and smoothing

In the CONIOPOL algorithm, only the portion of the attenuated backscatter profile exhibiting a sufficiently high signal-to-noise ratio (SNR) is considered. The noise level is estimated over a time interval of 30 minutes in an altitude range where no aerosols or clouds are expected, using the SNR preprocessing method of Morille et al. (2007) with a threshold set at 3. Noise calculations are performed within the range gates spanning 14,760 to 15,720 m. The XPOL and PPOL profiles are subsequently mirror-filtered using the SNR-filtered attenuated backscatter profile as a reference. To reduce high-frequency noise while preserving the main spatiotemporal structures of the CL61 signal, a two-dimensional Gaussian smoothing was applied on the attenuated backscatter, XPOL, and PPOL signals. A Gaussian kernel with standard deviations of (3.0, 3.0) samples in time and range is used, which—given the CL61's 30 s temporal resolution and 4.8 m vertical resolution—corresponds to an effective smoothing window of approximately 9 min in time and 86 m in the vertical dimension.

4.3 Threshold classification and validation

Classification of atmospheric targets as aerosols or clouds/precipitation is based on a threshold applied to the attenuated backscatter signal. A signal is identified as precipitation when the threshold is exceeded throughout more than 80% of the vertical range between the ground and the cloud base height retrieved by the CL61. The flowchart illustrating CONIOPOL's precipitation detection process is shown in Fig. 3.

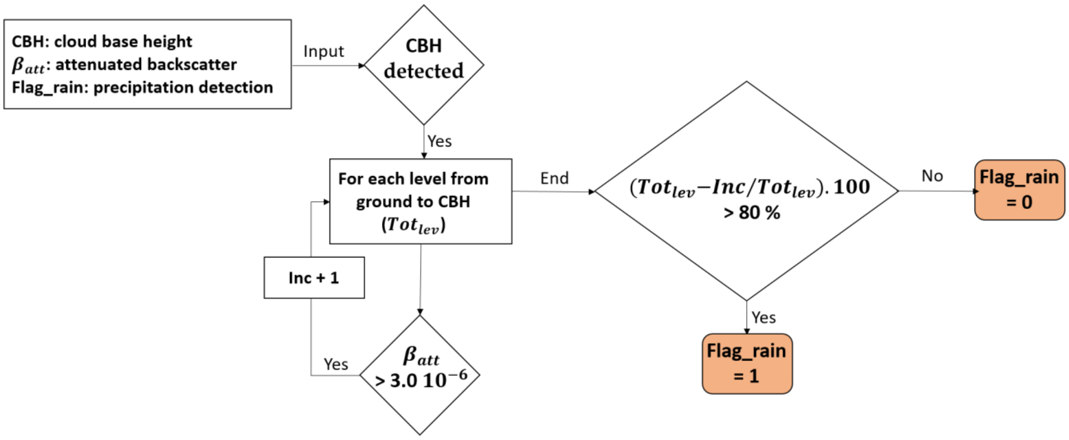

Figure 3: Decision tree employed in CONIOPOL for the detection of precipitation events. The flowchart illustrates the logical sequence of conditions applied to the attenuated backscatter profiles from the CL61 ceilometer.

The threshold for distinguishing aerosols from clouds and precipitation is determined based on the ratio of the relative frequency distributions of attenuated backscatter values observed with and without clouds or precipitation, with the threshold corresponding to the point where this ratio exceeds 1. Figure 4 shows these relative frequency distributions and their corresponding ratios for the months of May and September.

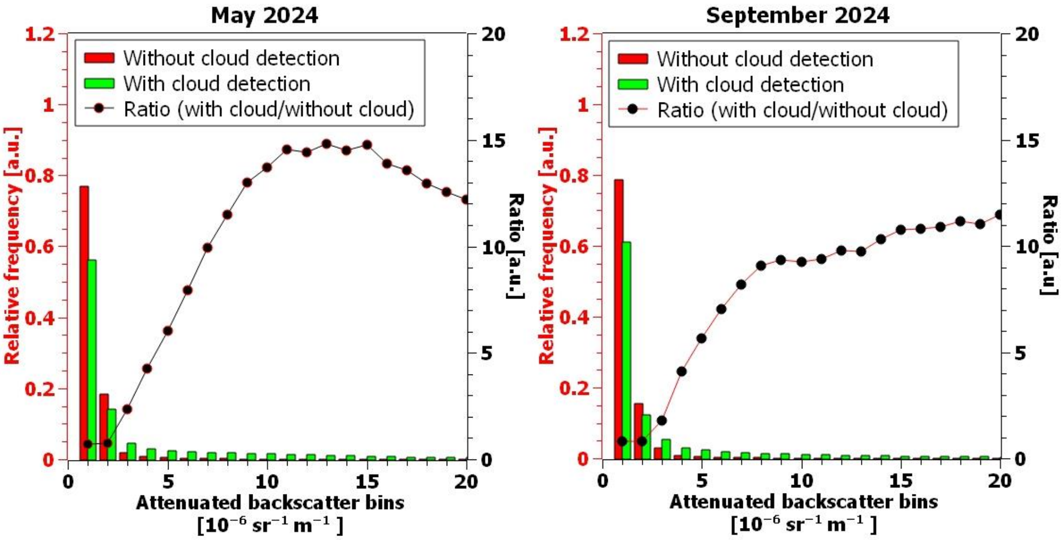

Figure 4: Relative frequency distributions (left y-axis) of attenuated backscatter values with (green) and without (red) cloud detection for May 2024 (left) and September 2024 (right). The black dots represent the ratio of distributions with and without clouds (right y-axis). The threshold for distinguishing clouds from clear-sky conditions corresponds to the point where this ratio exceeds 1.

Higher backscatter values occur more frequently in the presence of clouds or precipitation, whereas lower values are generally associated with clear-sky conditions. At Uccle, one year of data yielded a threshold of 3×10−6 sr−1m−1, which was consistent across months as illustrated partially in Fig. 4, and aligns with the value reported by Van Tricht et al. (2014) for distinguishing clear and cloudy conditions using ALCs (CT25K and CL31) operating at a wavelength similar to the CL61. This threshold is lower than 10−5 sr−1m−1 reported by Manninen et al. (2018) and 5×10−5 sr−1m−1 used by Harvey et al. (2013) for cloud detection with the Halo Photonics Streamline Scanning Doppler Lidar.

Applying this threshold to other CL61 instruments within CONIOPOL requires accurate calibration of the attenuated backscatter signal and regular maintenance of the instrument window. Nevertheless, this threshold may limit the detection of aerosol plumes with cloud-like opacity, potentially leading to their misclassification as clouds. This issue is particularly pronounced near sources of aerosol emissions. In volcanic regions, for example, ash fall may also be erroneously classified as snow precipitation.

The validity of precipitation detection using this threshold was assessed by comparing monthly detection frequencies from CONIOPOL with those recorded by a rain gauge (OTT Pluvio1, OTT Hydromet) installed near the CL61 (Fig. 5) in Uccle. Between February and September, gauge-based precipitation occurrence was generally equal to or slightly higher than that of CONIOPOL, likely due to the coarser temporal resolution of the gauge (1 h) relative to CONIOPOL (10 min). From October onwards, a marked discrepancy emerges, which cannot be attributed to temporal resolution differences but rather to an increase in fog and mist events during winter, except in February 2024, when fog occurrence was minimal due to unusually warm and rainy conditions. In such cases, fog, mist, or drizzle were prone to being misclassified as precipitation by CONIOPOL. This limitation was not further investigated, as CONIOPOL development primarily focused on aerosol identification through the separation of aerosols from fog, mist, drizzle, and precipitation. To enhance discrimination between precipitation/drizzle and fog/mist, it is recommended to combine the ALC with an additional ground-based remote sensing instrument, such as a Doppler radar (Acquistapace et al., 2019; O'Connor et al., 2005) or a Doppler wind lidar with a depolarization channel such as the Halo Photonics Streamline (Le et al., 2024).

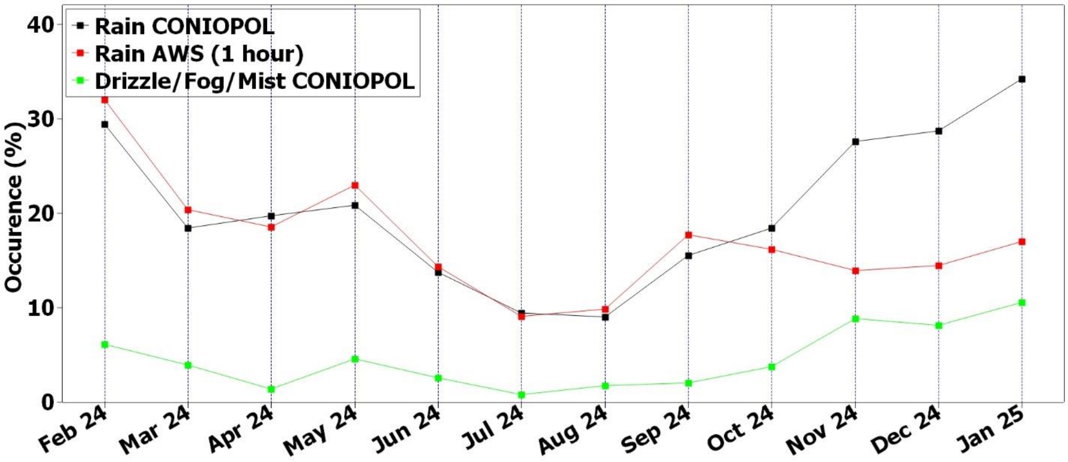

Figure 5: Monthly occurrence of precipitation events detected by CONIOPOL and by the automatic weather station (AWS) from February 2024 to January 2025. Black: rain (CONIOPOL); red: rain (AWS, 1 h resolution); green: drizzle/fog/mist (CONIOPOL).

4.4 Depolarization ratio

After separating aerosols, clouds, and precipitation, the identification of aerosols can be further refined using the Linear Depolarization Ratio (LDR), which provides essential, although not comprehensive, quantitative information for aerosol classification (Comerón et al., 2017). High LDR values (greater than 0.2) are typically associated with non-spherical particles such as volcanic ash or mineral dust (Groß et al., 2012). In contrast, values close to 0 indicate spherical particles, such as marine aerosols, while intermediate values reflect mixtures of spherical and non-spherical particles.

Although LDR is a powerful indicator of particle sphericity, it cannot uniquely identify aerosol type on its own. A more robust classification requires the use of dual-wavelength lidar and polarized channels to retrieve additional optical parameters such as the lidar ratio and the Ångström exponent, which provide complementary information on aerosol size and composition. When using only LDR to classify aerosols, parameters like aerosol size distribution, aspherical aerosol orientation, mixture of aerosol types, hydroscopic growth and multiple scattering effects can impact the LDR and lead to ambiguous identification. To address this, methodological choices must be made, which aim to minimize misclassification by ensuring that each aerosol type is identified consistently, even when their depolarization signatures partially overlap. Aerosols are thus classified using an explicit category.

The CONIOPOL classification relies on measurements conducted during a field campaign in Cardington, UK, between March and September 2020, using approximate depolarization ratio ranges associated with different scattering types, as reported in the Vaisala white paper (VAISALA, 2021).

Although volcanic ash and mineral dust may exhibit overlapping LDR values, they are treated as distinct categories to prevent double classification. This methodological choice ensures the robustness and internal consistency of the CONIOPOL classification. However, this choice inevitably entails a degree of uncertainty in situations where the true aerosol type cannot be resolved from depolarization alone. For this reason, the optimal application of the algorithm in contexts of volcanic eruptions require integration of complementary constraints, including geographical source attribution, air mass back trajectory analysis, and, where available, additional optical parameters.

To ensure a consistent classification of smoke and marine aerosols, and to better delineate smoke plumes, a threshold on the parallel backscatter (PPOL) is applied when the LDR is lower than 0.1. This methodological choice prevents the misclassification of smoke in regions where other aerosol mixtures are present. When the threshold is not met but the LDR values remain within this range, CONIOPOL classifies the particles as hygroscopic aerosols.

This threshold was defined based on the ratio between the frequency distribution of PPOL values during a period affected by smoke plume events and the frequency distribution observed during a reference period without smoke plumes. The criterion for threshold selection was that this ratio exceeded unity above 2000 m. For the Uccle site, the ratio was computed using observations from the last 15 days of August 2024—when the presence of significant smoke plumes was confirmed by CAMS—against the first 15 days of August, serving as the reference period without smoke influence, as illustrated in Fig. 6. The resulting threshold value was set to 1.0×10−6 sr−1m−1, corresponding to the PPOL value at which the ratio consistently exceeded 1. To ensure that this effect was specifically attributable to smoke and not to background variability, the frequency distribution was also analyzed below 2000 m for both periods, where no substantial differences were observed, confirming that the observed signal enhancement was restricted to altitudes impacted by transported smoke. Furthermore, the robustness of this approach was tested on several control months without smoke intrusions (such as April 2024). In this case, no significant differences were found between the frequency distributions at the beginning and end of the month, both below and above 2000 m, thereby supporting the methodological validity of the threshold definition. Overall, this procedure strengthens the statistical reliability of the classification framework by minimizing the likelihood of false positives arising from natural variability in the aerosol background.

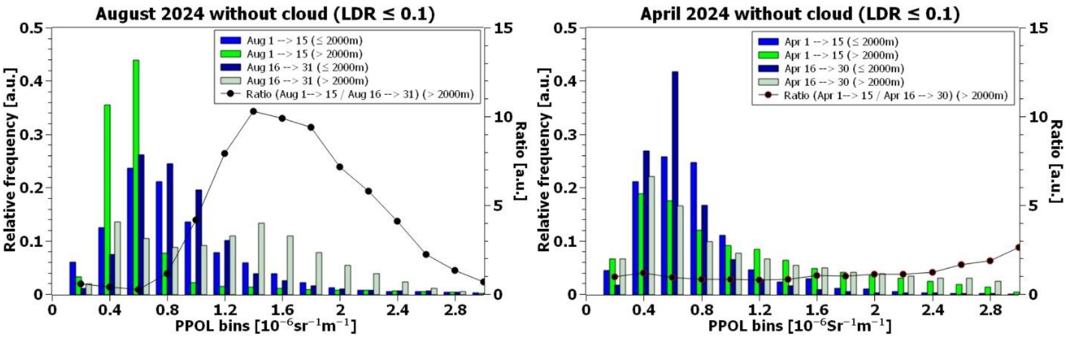

Figure 6: Relative frequency distributions of the parallel-polarized signal (PPOL) for two periods without cloud contamination (LDR <= 0.1): (left) August 2024 and (right) April 2024. Colored bars represent distributions for different sub-periods and altitude ranges below and above 2000 m. Specifically, blue denotes the first 15 days of the month below 2000 m, green the first 15 days above 2000 m, grey the last 15 days below 2000 m, and pink the last 15 days above 2000 m. The black points indicate the ratio of the relative frequency between the last 15 days and the first days of the month for altitudes above 2000 m.

For LDR values between 0.1 and 0.2, aerosol type attribution is inherently uncertain, as this interval represents a transition zone where particles of different morphologies and sizes can coexist and collectively shape the LDR. Such values may arise from external mixing of spherical and non-spherical particles or from internally mixed aerosols with variable shape characteristics. Moreover, biological particles such as pollen frequently exhibit depolarization ratios within this range, adding further ambiguity. For this reason, this interval is treated as a mixed-aerosol category rather than being assigned to a single, well-defined aerosol type.

At cloud level, the distinction between spherical liquid droplets and non-spherical ice crystals is generally unambiguous due to their markedly different scattering properties. However, in optically thick liquid clouds, multiple scattering effects can artificially enhance the LDR signal. This phenomenon justifies extending the classification of liquid water droplets up to an LDR value of 0.23, which corresponds to the upper limit defined for ice crystals.

At the precipitation level, classification is inherently more challenging, particularly for phenomena involving small water droplets such as drizzle, fog, and mist. Multiple scattering in these droplets can lead to artificially elevated LDR values, potentially resulting in misclassification as rain. This limitation has been noted previously and was not further investigated, as CONIOPOL was primarily designed for aerosol detection rather than detailed precipitation analysis. Furthermore, no intermediate category (e.g., mixed snow) was introduced between rain and snow to maintain a parsimonious classification scheme at the precipitation level.

4.5 2D grid-based clustering

The density-based spatial clustering of applications with noise (DBSCAN) algorithm is applied to a two-dimensional grid to identify coherent clusters corresponding to distinct target types (Bhattacharjee and Mitra, 2020; Ester et al., 1996), considering only detections exceeding a predefined threshold. This clustering approach is particularly effective for filtering out statistically insignificant or isolated detections, thereby reducing the likelihood of false alerts and enhancing the reliability of aerosol identification. The grid is constructed with temporal and vertical resolutions of 150 s and 24 m, respectively, providing sufficient granularity to capture the structure of observed plumes or layers. A density threshold of 0.4 is employed to ensure that only regions with a sufficiently concentrated occurrence of detections are retained as meaningful clusters, further strengthening the physical relevance of the classification.

4.6 Showcase

To illustrate the practical application of the CONIOPOL classification framework, Fig. 7 presents a representative example of its output applied to CL61 measurements acquired on 16-17 February 2024. The example showcases how the algorithm interprets the raw attenuated backscatter and LDR signal to produce a temporally and vertically coherent categorization of atmospheric aerosols and hydrometeors. During the previous night and the early morning hours of 16 February, CONIOPOL detected an elevated dust plume situated near the top of the boundary layer. The plume exhibited weak coupling with the underlying boundary layer, allowing a portion of the dust to mix with background aerosols of the boundary layer. This interaction was accordingly classified as aerosol mix. Importantly, the plume remained aloft and did not affect surface air quality. The plot also contains multiple cloud layers with distinct microphysical properties. CONIOPOL clearly discriminated an upper layer composed of ice crystals and a lower layer composed of supercooled liquid water, reflecting the vertical complexity of the cloud field. Precipitation features were also captured: shortly before 07:00 UTC, the algorithm identified a snow–rain transition near 2200 m. Overall, this example highlights the capability of CONIOPOL to extract fine-scale atmospheric structure from single-wavelength lidar measurements and to provide a detailed and physically consistent depiction of aerosol, cloud, and precipitation processes.

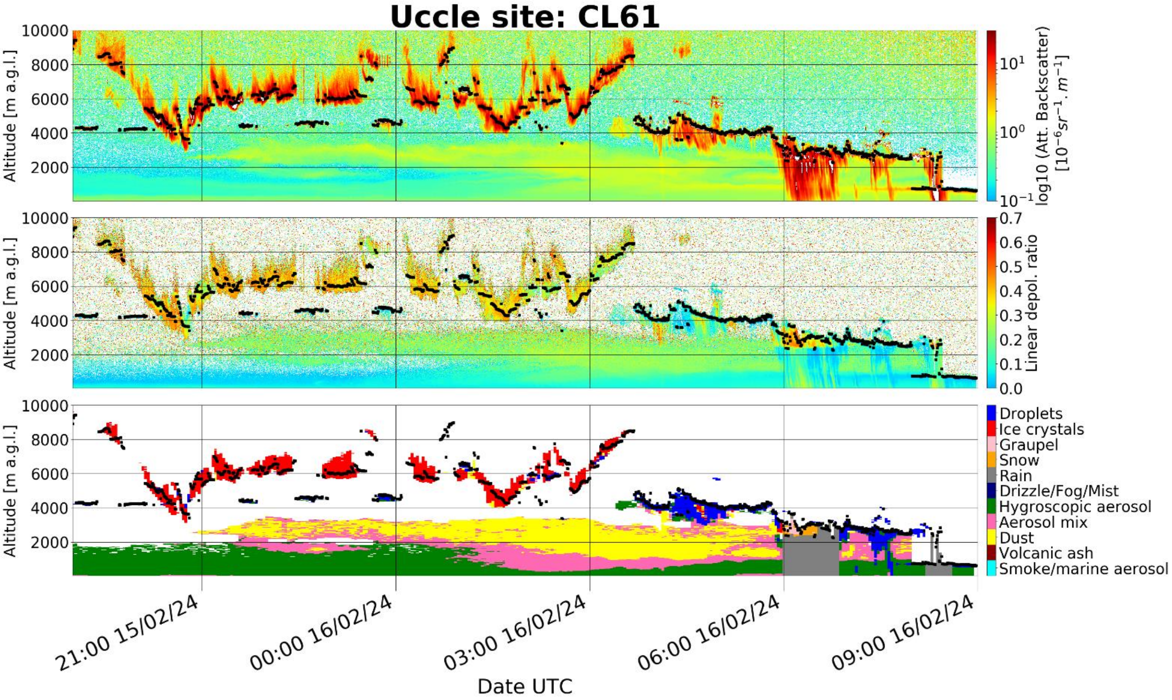

Figure 7. Raw attenuated backscatter (top) and LDR (middle) observed during the night of 15–16 February 2024 in Uccle with the CL61, shown as a function of altitude and time, together with the corresponding CONIOPOL classification (bottom). The classification panel displays the identified aerosol types, hydrometeors, and cloud phases. Black dots indicate the detected cloud-base height.

5 CAMS Global Forecast

The Copernicus Atmosphere Monitoring Service (CAMS) Global Forecast provides daily near-real-time predictions of atmospheric composition, including aerosols and reactive gases, on a global grid (Flemming et al., 2015; Peuch et al., 2022). Forecasts are produced using the ECMWF Integrated Forecasting System, which couples meteorology with aerosol and chemistry modules. Two forecast cycles are issued per day at 00 UTC and 12 UTC, each with a native temporal resolution of 3 hours and extending up to five days. In this study, only the first 12 hours of each forecast cycle were used.

CAMS forecast data were employed to validate the aerosol detections from CONIOPOL by comparing observed events with corresponding CAMS outputs. Key aerosol species from CAMS used in this study include total dust (0.03–20 µm) mixing ratio, total sea salt (0.003–20 µm) mixing ratio, total soot (hydrophilic + hydrophobic black carbon) mixing ratio, total organic carbon (hydrophilic + hydrophobic organic matter) mixing ratio, and sulfate aerosols mixing ratio (Benedetti et al., 2009; Morcrette et al., 2009; Rémy et al., 2019).

https://doi.org/10.5194/egusphere-2026-948
Preprint. Discussion started: 21 April 2026

Compared to the CAMS reanalysis, which provides a consistent retrospective dataset optimized for climate studies and long-term trend analysis, the forecast product is better suited for short-term monitoring of wildfire smoke, dust events, and air quality. Moreover, the reanalysis was not available at the start of this study, making the forecast product the best option for timely analysis.

6 Results

6.1 CONIOPOL output analysis

The analysis of CONIOPOL output was carried out over a complete annual cycle, with particular emphasis on the lowest 5000 m of the atmosphere. This vertical range was selected because the majority of detection and classification events were concentrated within the atmospheric boundary layer and in the adjacent lower free troposphere for the study period, where most aerosol–cloud–precipitation interactions occur and where the strongest seasonal variability is expected. This altitude limitation did not permit a complete analysis of cloud phase, since higher-level ice and mixed-phase clouds may extend well above the 5000 m threshold and are therefore not fully represented in the dataset. Nevertheless, the objective of this analysis is not to provide an exhaustive description of cloud microphysics, but rather to highlight the capabilities and potential inconsistencies in the CONIOPOL output, particularly in the aerosol classifications.

6.1.1 Occurrence analysis

Figure 8 presents the monthly distribution of aerosol, cloud phase and solid precipitation occurrences throughout the study period. It is a temporal occurrence in which several categories can be detected simultaneously within the same time frame. Such overlaps arise because different targets may coexist within the atmospheric column. Consequently, the summed occurrences of all categories may exceed 100%. The classifications were organized into two broad families: depolarizing aerosols and ice crystals, and low-depolarizing aerosols. In addition, solid precipitation was separated from liquid droplets (liquid precipitation already shown separately in Fig. 5). It is noteworthy that depolarizing targets did not exhibit a background occurrence signal with a consistent evolution across the different identified categories. This absence of coherence suggests that the observed variability is not an artifact of the adopted methodology but rather reflects genuine differences in the optical properties of the detected aerosol and cloud particles.

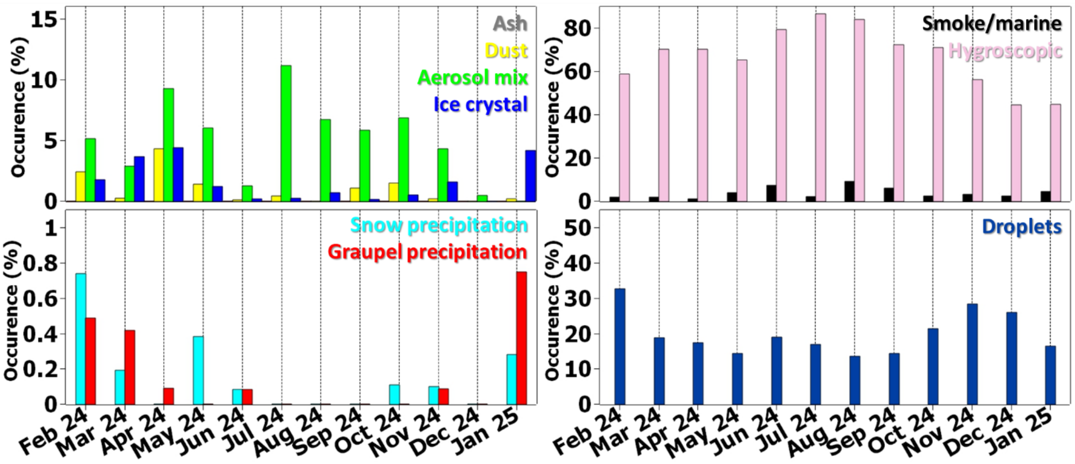

Figure 8: Monthly occurrence (%) of the different CONIOPOL-detected classes between February 2024 and January 2025. Top-left panel: Occurrence of ash, dust, aerosol mixing, and ice crystal classes. Bottom-left panel: Occurrence of solid precipitation classes, including snow and graupel. Top-right panel: Occurrence of hygroscopic and smoke/marine aerosol categories. Bottom-right panel: Occurrence of liquid droplets.

Throughout the year, hygroscopic aerosols classification was most frequently observed, with annual occurrences consistently exceeding 50% and reaching peaks of approximately 80% in July and August. The second most prevalent category was represented by mixed aerosols, with distinct seasonal maxima recorded in March, June, and August 2024, reaching up to ~12%. Dust was observed at moderate frequencies, primarily during spring (March–April) and summer (June–August). By contrast, smoke and marine aerosols were persistently detected at low levels, generally accounting for less than 5% of observations. No ash was detected, while ice crystals were recorded particularly during winter, early spring and late autumn period. By contrast, summer months were characterized by very limited ice crystal occurrence.

With regard to precipitation, both snow and graupel were observed only sporadically (<1%), with isolated peaks in February, March, and January. Snow was generally detected more frequently than graupel, except in January 2025, when a pronounced peak of graupel occurrence was recorded. Liquid droplet occurrence was characterized by greater variability, with annual occurrences ranging between ~20% and 35%. Distinct peaks were observed in February and November 2024, corresponding to periods of enhanced precipitation frequency as illustrated in Fig. 5.

6.1.2 Vertical cumulative analysis

The examination of the vertical distribution of each target type in relation to its seasonal variability provides valuable insight into both the dominant altitude ranges and their temporal evolution of occurrence throughout the year. To this end, Fig. 9 presents the normalized cumulative occurrence for each month in which significant detections were recorded for the different aerosol categories and for ice crystals. The use of cumulative occurrence profiles is particularly advantageous, as they yield a normalized measure of the vertical extent of each category, thereby enabling direct comparisons between months with different detection frequencies and minimizing biases introduced by unequal sampling. Beyond their utility in this study, such profiles are widely employed in lidar-based research to investigate the vertical structure of aerosols and hydrometeors (Baars et al., 2012; Illingworth et al., 2007), as they provide a robust framework for evaluating both seasonal variability and the reliability of CONIOPOL's classification.

Dust events predominantly originated at higher altitudes in February and May, and at lower altitudes in April and October, with September and May exhibiting pronounced vertical gradients over narrower altitude ranges. Normalized cumulative occurrence curves for dust asymptotically approach unity, indicating that all detected dust plumes remained below 5000 m. In contrast, ice crystals were observed at higher altitudes than dust and did not exhibit an asymptotic limit, suggesting their presence above 5000 m.

For the aerosol mixing category, below 200 m, a comparable normalized cumulative occurrence growth rate was observed across all months except September, November, and December. At higher altitudes, this growth persisted in March and August, gradually approaching an asymptotic value near 2000 m. For February, April, May, July, and October, the growth rate was lower before reaching the asymptotic limit above 2000 m, remaining generally below that of dust. Conversely, in June, September, November, and December, aerosol mixing was predominantly detected at higher altitudes.

At the hygroscopic category level, seasonal variability was evident, with the asymptotic altitude limit reached more rapidly in winter than in summer. This likely indicates that hygroscopic aerosols were largely confined to the atmospheric boundary layer, particularly since this limit was lower than that observed for dust. Smoke and marine aerosols were likewise mostly restricted to the lower atmospheric boundary layer, with approximately 80–90% of cumulative occurrences below 800 m. Exceptions occurred in June and August, when the asymptotic limit extended above 2000 m.

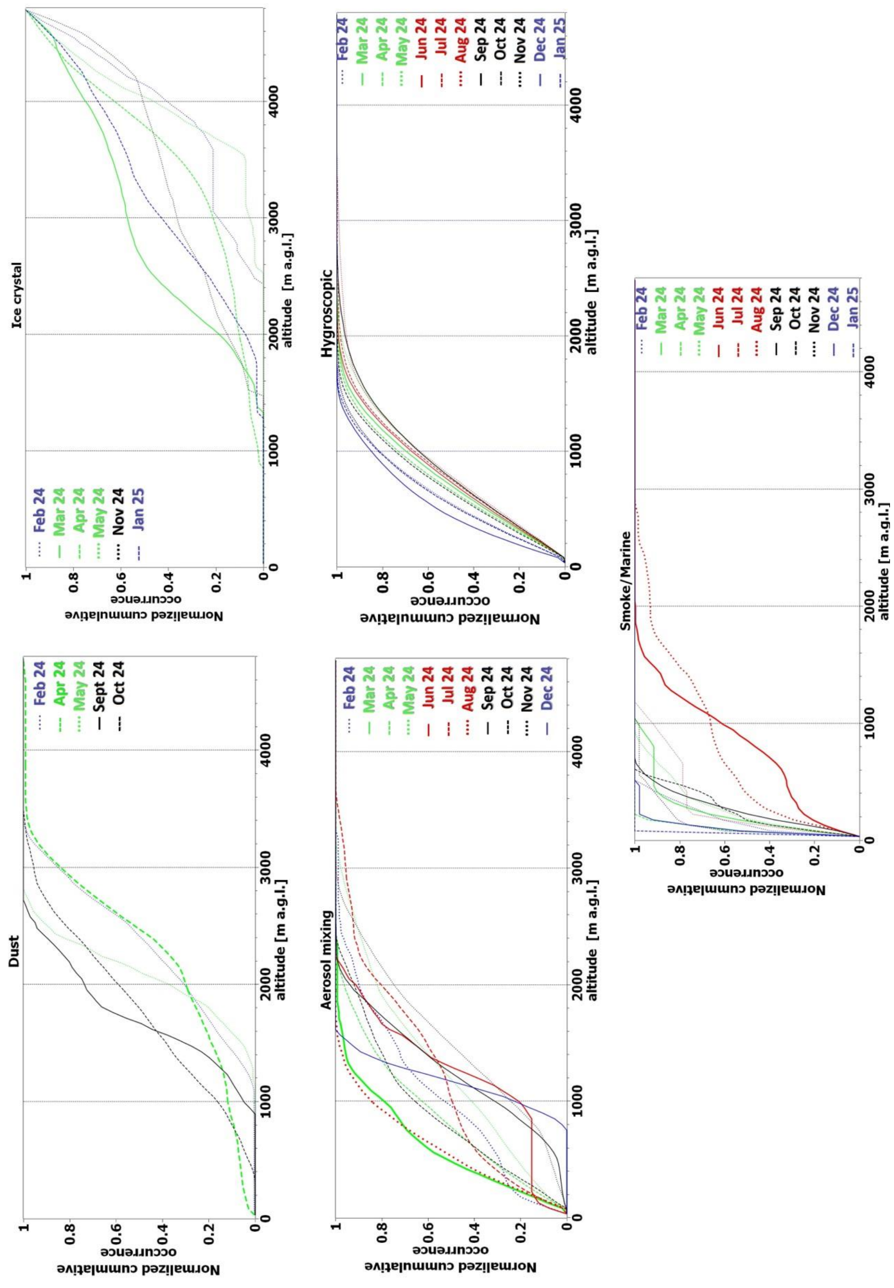

450 **Figure 9: Normalized cumulative occurrence of the different aerosol classifications as a function of altitude for selected months of 2024 and 2025 (shown only when the monthly occurrence exceeds 1%). Blue corresponds to winter months, green**

to spring months, red to summer months, and black to autumn months. Within each seasonal group, the first month is represented by a solid line, the second month by a dashed line, and the last month by a dotted line.

6.2 Intercomparison with CAMS forecast

The comparison of CONIOPOL outputs with model simulations is considered a key step in the assessment of data consistency, while it is recognized that models do not represent ground truth and may be affected by uncertainties in emissions, transport, and parameterizations. Nevertheless, spatially and temporally continuous fields are provided by models, which can be used as a valuable reference for the validation of site-specific observations, as has been demonstrated in previous studies (e.g. Eskes et al., 2024; Flentje et al., 2021). Due to differences in time and vertical resolution, a direct comparison between absolute model outputs and CONIOPOL results cannot be performed, since CONIOPOL does not provide quantitative aerosol concentrations but only indicates the presence or absence of the most depolarizing aerosol types. To address this limitation, the distribution of CAMS values (from the vertical-profile grid point closest to the Uccle site) was assessed conditionally on CONIOPOL detections in both time and altitude, thus providing a consistent basis for intercomparison, despite the differing natures of the datasets. In this analysis, CONIOPOL data were aggregated at an hourly resolution and a vertical range bin size of 48m. Each aerosol category was considered detected when its recurrence exceeded 60% within the hour and undetected otherwise, for each vertical range bin. Each CAMS value for a given aerosol category was consequently used at least three times in the analysis by associating it with the closest vertical ranges from the CONIOPOL dataset.

To further evaluate the ability of CONIOPOL to discriminate between depolarizing aerosol classes and ice crystals, the distribution of total dust CAMS values for cases in which neither depolarizing aerosols nor ice crystals were detected by CONIOPOL was used as a reference. This reference distribution was then compared with those associated with the detection of the different depolarizing categories below and above 1000m, thereby establishing an indirect validation framework.

Figure 10A-B presents box plots of total dust CAMS distributions for each depolarizing aerosol and ice crystal category alongside the reference distribution for cases without depolarizing aerosols or ice crystals. The plots summarize key statistics—including medians, interquartile ranges, and outliers—facilitating visual assessment of differences between categories and the reference.

Reference cases, with no depolarizing aerosols or ice crystals detected, exhibited a very low median (0.4×10^{-9} kg kg^{-1}), confirming that CONIOPOL did not miss major dust episodes simulated by CAMS. Dust detections showed substantially higher medians, with 98.8×10^{-9} kg kg^{-1} below 1000 m and 124.1×10^{-9} kg kg^{-1} above 1000 m. Although the two medians were comparable, values below 1000 m displayed a broader spread toward zero, suggesting either limitations in CONIOPOL's dust detection or underestimation of dust episodes in CAMS forecasts. The aerosol-mix category displayed intermediate medians—8.4×10^{-9} kg kg^{-1} below 1000 m and 46.3×10^{-9} kg kg^{-1} above 1000 m—consistent with mixtures of dust and other aerosol types. Ice-crystal category showed very low medians (2.1×10^{-9} kg kg^{-1}), similar to the reference, confirming that most detections were not misclassified as dust episodes. A closer look

https://doi.org/10.5194/egusphere-2026-948
Preprint. Discussion started: 21 April 2026

at April 2024 (Fig. 10C-D)—characterized by several intense dust episodes—reveals a particularly strong signal in the dust category above 1000 m, with a median of 190.9 × 10^{-9} kg kg^{-1}, clearly distinct from the other categories. Notably, some ice-crystal detections during this period coincided with CAMS-modeled dust episodes, suggesting occasional coexistence or mixing of these categories.

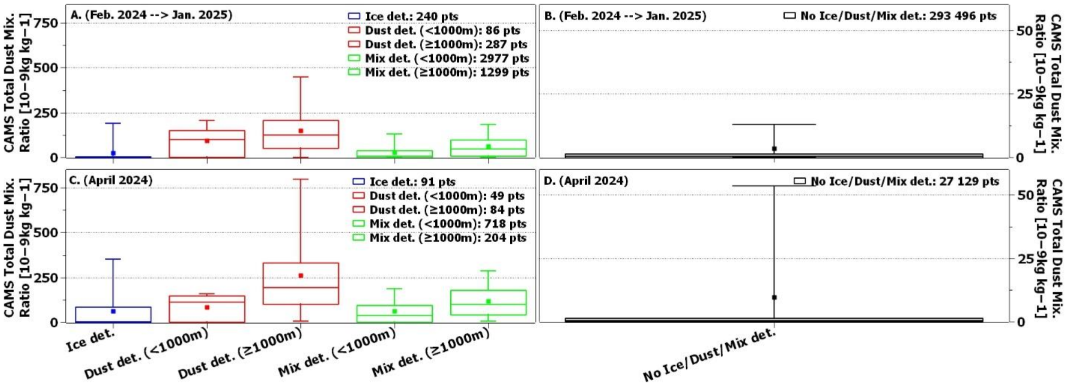

Figure 10: Box plots of CAMS total dust mixing ratio (10^{-9} kg kg^{-1}) corresponding to the different depolarizing aerosol categories detected by CONIOPOL between February 2024 and January 2025 (A) and for April 2024 (C). The left panel shows the distributions for ice crystals (blue), dust below and above 1000 m (red), and aerosol mixing below and above 1000 m (green). The right panel shows the reference distribution corresponding to cases where no depolarizing aerosols or ice crystals were detected by CONIOPOL between February 2024 and January 2025 (B) and for April 2024 (D). Each box represents the interquartile range (25th–75th percentile), the horizontal line inside the box indicates the median (50th percentile), and the square marker denotes the mean value. Whiskers extend to the 5th and 95th percentiles. The number of data considered for each detected category is indicated.

Regarding the detection of marine smoke/aerosols, Fig. 11A-B-C-D compares the different box plots of CAMS outputs—namely total sea salt, total soot, sulfate, and total organic—between cases where CONIOPOL did not detect marine smoke/aerosols (used as the reference) and cases with positive detections, analyzed separately below and above 1000 m. All reference medians were close to zero, except for total sea salt at both altitude ranges and for sulfate below 1000 m. For total sea salt, no significant differences were observed between detection and non-detection cases, either below or above 1000 m. Focusing on August (Fig. 11E-F), a month marked by the passage of several smoke plumes, a clear difference emerges between the reference and the CONIOPOL detections of marine/smoke aerosols for sulfate (median: 9.6 × 10^{-9} kg kg^{-1}), total organic (median: 11.9 × 10^{-9} kg kg^{-1}) and total soot (median: 1.0 × 10^{-9} kg kg^{-1}) above 1000 m. In contrast, below 1000 m, reference and detection cases show comparable values.

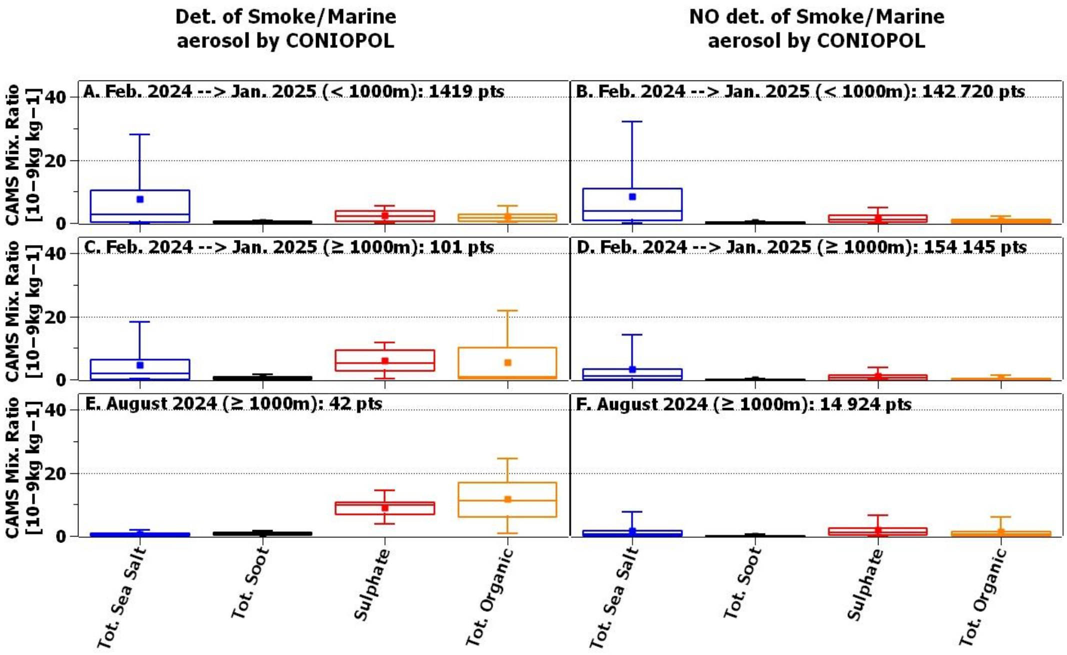

Figure 11: Box plots of CAMS mixing ratio (10^{-9} kg kg^{-1}) corresponding to the total sea salt (blue), total soot (black), sulphate (red) and total organic (orange) corresponding to periods when smoke/marine aerosols were detected by CONIOPOL (left panel) between February 2024 and January 2025 below 1000 m (A) and above 1000m (C), and for August 2024 above 1000m (E). The right panel corresponding to periods when no smoke/marine aerosols were detected between February 2024 and January 2025 below 1000 m (B) and above 1000m (D), and for August 2024 above 1000m (F). Each box represents the interquartile range (25th–75th percentile), the horizontal line inside the box indicates the median (50th percentile), and the square marker denotes the mean value. Whiskers extend to the 5th and 95th percentiles. The number of data points corresponding to each detection condition is indicated.

7 Discussions

Overall, the results highlight clear seasonal and vertical patterns in the occurrence and distribution of aerosols and hydrometeors over the study site, as well as a generally consistent correspondence between CONIOPOL detections and CAMS model outputs. The analyses collectively indicate that depolarizing aerosols such as dust and mixed aerosols exhibit distinct altitude-dependent signatures and temporal variability, while hygroscopic and low-depolarizing aerosols remain largely confined to the boundary layer. Despite inherent limitations related to the use of the LDR-only classification and differences in temporal and vertical resolutions between datasets, the intercomparison confirms the robustness of the detection methodology. It should also be noted that these findings are based on a single-site, one-year dataset, which limits their representativeness but provides an unprecedented temporally continuous record for the region. With the aim of further validating CONIOPOL, the following discussion places these findings in the context of previous studies, exploring the physical and meteorological processes underlying the observed seasonal patterns and altitude dependencies.

7.1 Depolarizing targets

Comparing our results with previous studies conducted in Western and Central Europe remains challenging. First, the aerosol classification scheme employed in our analysis does not perfectly align with those used in other studies, making direct comparisons difficult. Second, unlike many earlier works that rely on campaign-based or discontinuous datasets, our study provides continuous, uninterrupted temporal coverage, which helps reduce potential sampling biases. Moreover, to our knowledge, no study covering the entire year 2024 has yet been published for Western and Central Europe, limiting the availability of recent reference data. Nevertheless, despite natural variability, previous studies can serve as useful benchmarks for assessing whether the characteristics of the aerosol categories detected by CONIOPOL are consistent with earlier observations. For the dust category, the altitudes of the plumes detected by CONIOPOL fall within the range observed at Palaiseau, with heights between 400 m and 4,000 m (Papayannis et al., 2008). Regarding the seasonality of dust plumes, our study shows the highest occurrences in February, March, May, September, and October, rather than during the summer months. This contrasts with Marinou et al. (2017), who reported stronger dust activity over Central and Western Europe during spring and summer, based on a nine-year dataset that provides a more robust climatological reference than our one-year analysis. In our case, the highest frequency of the “mixed aerosol” category occurred in June, which may correspond to one or more dust intrusion events combined with other aerosol types. This interpretation is consistent with the CAMS intercomparison analysis, which indicates that the “mixed aerosol” category was associated with noticeably higher CAMS dust mixing ratio values compared to periods without depolarizing target detections, particularly above 1000 m. However, these values remained well below those observed when CONIOPOL explicitly detected dust, suggesting that the “mixed aerosol” class likely represents episodes of partial or diluted dust intrusions combined with other aerosol types. Such mixing becomes increasingly pronounced with the atmospheric transport distance from the source region (Dall’Osto et al., 2010). Furthermore, it is also possible that dust transport toward Western Europe was reduced in 2024, due to more efficient removal processes and large-scale circulation patterns (e.g., Schepanski et al., 2009) that favored eastward transport. Indeed, Ionita and Nagavciuc (2025) reported that the summer of 2024 was marked by unprecedented heatwaves and exceptionally dry conditions in Eastern Europe, linked to a persistent high-pressure system over the eastern continent and a low-pressure anomaly over the central North Atlantic (Ionita et al., 2025). These synoptic features likely enhanced the eastward advection of Saharan dust while limiting its transport toward Western Europe. It should also be noted that some dust episodes may remain undetected when plumes are located above optically thick clouds or mixed within cloud layers, leading to an underrepresentation of such dust events in lidar-based classifications.

The observed difference in total dust mixing ratio detected by CONIOPOL between altitudes above and below 1000 m is consistent with known atmospheric processes. The amount of dust is generally lower near the surface due to gravitational settling, enhanced deposition, and the influence of boundary layer dynamics, including turbulence and frictional drag (Seinfeld and Pandis, 1998). Wet and dry removal processes further reduce near-surface dust accumulation during long-range transport. CAMS and similar global aerosol models often struggle to reproduce these near-surface concentrations accurately because of coarse vertical resolution, simplified boundary layer parameterizations, and uncertainties in deposition and transport processes (Huneeus et al., 2011; Zender et al., 2003), where virga processes can also play a key role enhancing vertical dust redistribution through sublimating precipitation and local turbulence (Karle et al., 2023). As a result, CAMS tends to underestimate—or even miss—dust below 1000 m while performing better at higher altitudes, where long-range transport dominates over surface removal. This likely explains why CONIOPOL consistently detected dust when dust CAMS mixing ratios near the surface was low compared to higher altitudes, and why some dust events detected by CONIOPOL were not captured by the CAMS model. Despite potential misalignments during plume onset and dissipation due to differences in temporal resolution between the two datasets, this temporal mapping appears robust, as periods with no depolarizing targets in CONIOPOL corresponded often closely to low or negligible dust concentrations in CAMS, indicating a limited impact of the resolution mismatch.

Although ice crystals were generally detected at much higher altitudes than dust plumes, intercomparison with CAMS reveals that, while dust mixing ratios are typically low during ice crystal detections, there is a notable spread toward higher values especially in April. This suggests occasional co-existence of dust and ice crystals, as previously observed by Chatziparaschos et al. (2025), who reported that Saharan dust contributes significantly to ice-nucleating particles in the atmosphere. Similarly, Brunner et al. (2021) demonstrated that mineral dust plumes can initiate ice crystal formation at cirrus altitudes, with these ice particles subsequently sedimenting through virga to lower atmospheric layers.

Notably, the “mixed aerosol” category detected by CONIOPOL during the spring months may also partially include pollen layers, which exhibit moderate depolarization signatures and occasionally display a diurnal detection pattern (results not shown; or provided in the Annex) characteristic of daytime pollen emissions. Several lidar studies have reported such diurnal patterns in pollen layers, aiding in their discrimination from other aerosol types (Bohlmann et al., 2019, 2021; Noh et al., 2013; Sicard et al., 2016). At the CL61 operating wavelength (~910 nm), typical particle linear depolarization ratios (LDR) associated with pollen range between 0.10 and 0.25, occasionally reaching up to 0.30 during intense episodes (Filioglou et al., 2023, 2025). These values are consistent with multi-wavelength lidar observations reporting pollen depolarization ratios of 0.05–0.15 at 355 nm, 0.20–0.45 at 532 nm, and ≤ 0.10 at 1565 nm, depending on species and morphology (Bohlmann et al., 2021; Cholleton et al., 2022). The moderate depolarization observed at 910 nm reflects the wavelength dependence of scattering by large, aspherical biological particles. Mixed layers containing both pollen and other aerosols typically yield intermediate depolarization values (~0.05–0.15), consistent with those observed in our “mixed aerosol” category during the main pollen season. This interpretation aligns with the temporal pattern of enhanced “mixed aerosol” detections in February, April, May, July, and October, corresponding to the main pollen emission period in Belgium (Hoebeke et al., 2018; Verstraeten et al., 2025; de Weger et al., 2021). However, the dip observed in June does not correspond precisely to the transition between tree and grass pollen emissions—usually occurring in May (Hoebeke et al., 2018)—and may instead reflect the influence of other aerosol types or meteorological variability. Moreover, given the large diversity in pollen size, shape, and optical properties, not all pollen events are necessarily captured within this category. The observed gap in June is also unlikely to result from misclassification of pollen as dust, since dust occurrences were minimal during this month. This uncertainty reflects an inherent limitation of single-wavelength polarization lidar systems, which may struggle to unambiguously discriminate weakly depolarizing biogenic particles, such as pollen, from other aerosol types exhibiting similar optical properties.

7.2 Weakly depolarizing targets

Automatic detection of weakly depolarizing targets using a single-wavelength lidar system remains inherently challenging. The intercomparison with CAMS below 1000 m proved less conclusive than for depolarizing targets in evaluating the robustness of CONIOPOL. This limitation is likely attributable, in part, to the complex processes occurring within the lowest layers of the atmosphere, which are frequently underrepresented in global models, including CAMS, as previously noted. This issue is particularly pertinent given that the majority of CONIOPOL detections of the smoke/marine aerosol category were confined to altitudes below 1000 m, where model uncertainties and the influence of near-surface processes are most pronounced.

Detection of marine or sea salt aerosols is especially challenging due to their weak depolarization signal, hygroscopic growth, and frequent mixing with other aerosol types within the atmospheric boundary layer. These factors significantly limit the sensitivity and classification accuracy of single-wavelength lidar systems such as CONIOPOL (Ferrare et al., 2023; Haarig et al., 2017; Klingebiel et al., 2019). The complex morphology and humidity-dependent size variability of sea-salt particles further increase optical retrieval uncertainties and may lead to partial misclassification with other weakly depolarizing aerosols (Ferrare et al., 2023; Haarig et al., 2017) .

However, above 1000 m, our results—particularly in August—demonstrated CONIOPOL's capability to detect smoke plumes. Corresponding CAMS outputs indicate that these plumes were often accompanied not only by soot but also by elevated concentrations of sulfate and total organic matter. This composition reflects the multiphase chemistry of biomass-burning aerosols, which release a mixture of black carbon, organic carbon, and sulfate precursors. These precursors undergo atmospheric oxidation to form secondary aerosols, thereby enhancing the total aerosol load at higher altitudes (Reid et al., 2005; Souri et al., 2017). The improved agreement between CONIOPOL and CAMS above 1000 m contrasts with the near –surface detections, where smoke/marine aerosols remain difficult to characterize. As with dust plumes, some smoke events at higher altitudes may remain undetected when the plumes are located above cloud layers or embedded within clouds, leading to potential underrepresentation of these events in the observations.

The so-called "hygroscopic aerosol" category in our classification likely includes a heterogeneous mixture of natural and anthropogenic fine-mode particles, encompassing both aged secondary aerosols and pollution-derived components. The seasonal behavior observed in our data—characterized by higher frequencies in summer relative to winter—closely aligns with established patterns across Europe (Freney et al., 2011; Mattis et al., 2008; Pio et al., 2007; Putaud et al., 2010). These studies consistently show that photochemical activity and secondary aerosol formation intensify during the warmer months, when elevated solar radiation and temperature accelerate oxidation of gaseous precursors, producing sulfates, nitrates, and secondary organic aerosols (SOA). Stagnant synoptic conditions and boundary-layer inversions further enhance aerosol residence time in the lower troposphere, amplifying the observed seasonal signal.

In addition, biogenic emissions play an increasingly important role in summer, as vegetation emits large quantities of volatile organic compounds (VOCs) that oxidize into low-volatility products contributing to the hygroscopic aerosol fraction (Varutbangkul et al., 2006). Both anthropogenic secondary aerosols and oxidized biogenic particles tend to exhibit near-spherical morphology, due to their liquid or semi-solid nature and hygroscopic properties.

Therefore, while the label “hygroscopic aerosols” might imply primarily water-soluble particles, our results suggest that this category more likely represents a complex mixture of quasi-spherical pollution-derived and biogenic secondary products dominating under photochemically active summer conditions. This interpretation reinforces the idea that seasonal aerosol variability in mid-latitude Europe is driven by both enhanced photochemistry and biospheric activity, rather than by hygroscopic growth alone.

8 Conclusion

The CONIOPOL algorithm, applied to single-wavelength lidar observations from the Vaisala CL61, provides a robust foundation for establishing a long-term and coherent climatology of aerosol occurrence and variability at a measurement site. While single-wavelength lidars inherently lack the spectral information required to fully resolve aerosol microphysical properties or to distinguish all aerosol types with high precision, their continuous temporal coverage, high vertical resolution, and operational reliability make them powerful tools for identifying recurrent aerosol regimes and their seasonal evolution. The resulting dataset offers a unique and consistent view of aerosol dynamics, effectively bridging the temporal gaps often encountered in satellite-based or multi-wavelength lidar observations.

The classification analysis performed with CONIOPOL demonstrates a robust capability to discriminate between major aerosol categories, including dust, smoke, mixed, and hygroscopic aerosols, despite the spectral limitation. In particular, the detection of dust and smoke plumes shows strong temporal and vertical coherence with CAMS model outputs, confirming the physical consistency of the classification algorithm and validating the system’s sensitivity to elevated aerosol layers. This agreement highlights the ability of single-wavelength lidar measurements to capture key aerosol transport events, such as Saharan dust outbreaks or long-range smoke intrusions, which are critical for understanding regional air quality and radiative impacts.

Beyond these major categories, the continuous dataset also reveals the complex variability of other aerosol types, such as hygroscopic and mixed layers, which are influenced by both anthropogenic and natural sources. The seasonal evolution of these classes—characterized by enhanced summer occurrence—reflects the interplay between photochemical activity, biogenic emissions, and meteorological conditions that modulate aerosol formation and growth. Despite the reduced spectral information, the temporal continuity of the ALC record enables the detection of such climatologically relevant patterns, providing key insights into aerosol–meteorology interactions.

In summary, while single-wavelength systems like CONIOPOL are spectrally constrained, their continuous operation, vertical profiling capability and demonstrated coherence with independent datasets (e.g., CAMS) make them indispensable components of regional aerosol monitoring networks. Their contribution is particularly valuable for building consistent, observation-based climatologies that complement both ground-based in situ measurements and global model simulations, thereby improving our understanding of aerosol sources, variability, and long-term atmospheric trends. The relatively low cost of polarized ALCs compared to multi-wavelength systems, combined with their straightforward 24/7 operational capability, makes CONIOPOL a valuable tool for air quality agencies. It enables real-time assessment of whether an aerosol plume interacts (especially dust plumes) with the ABL, and thus whether it may directly affect surface air quality. Such interactions are often challenging to represent accurately in atmospheric and air quality models, highlighting the importance of continuous ALC-based observations for improving model evaluation and forecasting.

However, the results presented here are derived from a single site, which, while representative, cannot by itself fully validate the CONIOPOL algorithm under diverse meteorological and aerosol conditions. Expanding the analysis to multiple sites equipped with Vaisala CL61 instruments—ideally covering different climatic and aerosol regimes—would provide a more comprehensive evaluation of the algorithm's performance and improve the robustness of its climatological applications.

Looking ahead, combining continuous ALC observations with complementary datasets—especially multi-wavelength and polarisation lidars—offers a clear path to improving aerosol typing and validation. In particular, EarthCARE's ATLID polarisation lidar will provide vertically resolved particle-type information that single-wavelength ALCs cannot retrieve. Joint use of CONIOPOL classifications with ATLID measurements would enable more rigorous validation of aerosol types and reduce uncertainties in mixed or weakly scattering layers. Further, the Royal Meteorological Institute is implementing an ACTRIS Aerosol In-Situ National Facility in Uccle and the respective boundary layer aerosol data will help to validate the CONIOPOL particle classification, in particular the aerosol scattering intensities and the size distribution data. Such synergies between various sensors will significantly enhance our ability to monitor aerosol variability, improve model evaluation—particularly within the boundary layer—and advance understanding of aerosol–cloud–radiation interactions relevant for both air quality and climate applications.

Data availability

The CL61 data that support the development and the validation of CONIOPOL are available from the corresponding author upon reasonable request. CAMS global atmospheric composition forecasts used in this study are available on the Copernicus Atmosphere Monitoring Service (CAMS) Atmosphere Data Store, DOI: 10.24381/04a0b097 (Accessed on 30-01-2025).

Author contributions

Q.L. developed CONIOPOL, conducted the full analysis, and drafted the manuscript. A.D. retrieved and prepared the CAMS data files to enable intercomparison with CONIOPOL output. All authors contributed to the discussion and writing of the document.

Competing interests

The authors declare that they have no conflict of interest.

Acknowledgements

We thank Reijo Roininen (Vaisala) for his sustained interest in the development of an algorithm such as CONIOPOL, aimed at classifying aerosols and hydrometeors using CL61 measurements. His technical input and discussions were highly appreciated. We also express our gratitude to Frans Fierens (Belgian Interregional Environment Agency, IRCEL - CELINE) for his interest and constructive feedback regarding the real-time operational use of CONIOPOL outputs, which helped reinforce the relevance of this work from an air-quality monitoring perspective. We further acknowledge colleagues who provided feedback and encouragement during the development of this algorithm. Many of these collaborations originated within the framework of the COST Action PROBE (CA18235, https://www.probe-cost.eu/). Although the Action has formally concluded, its network remains active: the collaborative spirit, scientific exchanges, and long-standing professional connections forged within PROBE continue to play a key role in ALC research across Europe. We are equally grateful to the community engaged in the E-PROFILE (https://e-profile.eu), where discussions and shared expertise have contributed to shaping and refining CONIOPOL.

Financial support

The research has been undertaken in the framework of the Solar-Terrestrial Centre of Excellence (STCE), funded by the Belgian Federal Science Policy Office. Q.L. is member of the Solar-Terrestrial Centre of Excellence.

References

Acquistapace, C., Löhnert, U., Maahn, M., and Kollias, P.: A New Criterion to Improve Operational Drizzle Detection with Ground-Based Remote Sensing, J. Atmospheric Ocean. Technol., 36, 781–801, https://doi.org/10.1175/JTECH-D-18-0158.1, 2019.

del Águila, A., Ortiz-Amezcua, P., Tabik, S., Bravo-Aranda, J. A., Fernández-Carvelo, S., and Alados-Arboledas, L.: Aerosol type classification with machine learning techniques applied to multiwavelength lidar data from EARLINET, Atmospheric Chem. Phys., 25, 12549–12567, https://doi.org/10.5194/acp-25-12549-2025, 2025.

Baars, H., Ansmann, A., Althausen, D., Engelmann, R., Heese, B., Müller, D., Artaxo, P., Paixao, M., Pauliquevis, T., and Souza, R.: Aerosol profiling with lidar in the Amazon Basin during the wet and dry season, J. Geophys. Res. Atmospheres, 117, https://doi.org/10.1029/2012JD018338, 2012.

Baars, H., Seifert, P., Engelmann, R., and Wandinger, U.: Target categorization of aerosol and clouds by continuous multiwavelength-polarization lidar measurements, Atmospheric Meas. Tech., 10, 3175–3201, https://doi.org/10.5194/amt-10-3175-2017, 2017.

Baars, H., Radenz, M., Floutsi, A. A., Engelmann, R., Althausen, D., Heese, B., Ansmann, A., Flament, T., Dabas, A., Trapon, D., Reitebuch, O., Bley, S., and Wandinger, U.: Californian Wildfire Smoke Over Europe: A First Example of the Aerosol Observing Capabilities of Aeolus Compared to Ground-Based Lidar, Geophys. Res. Lett., 48, e2020GL092194, https://doi.org/10.1029/2020GL092194, 2021.

Bedoya-Velásquez, A. E., Hoyos-Restrepo, M., Barreto, A., García, R. D., Romero-Campos, P. M., García, O., Ramos, R., Roininen, R., Toledano, C., Sicard, M., and Ceolato, R.: Estimation of the Mass Concentration of Volcanic Ash Using Ceilometers: Study of Fresh and Transported Plumes from La Palma Volcano, Remote Sens., 14, 5680, https://doi.org/10.3390/rs14225680, 2022.

Benedetti, A., Morcrette, J.-J., Boucher, O., Dethof, A., Engelen, R. J., Fisher, M., Flentje, H., Huneeus, N., Jones, L., Kaiser, J. W., Kinne, S., Mangold, A., Razinger, M., Simmons, A. J., and Suttie, M.: Aerosol analysis and forecast in the European Centre for Medium-Range Weather Forecasts Integrated Forecast System: 2. Data assimilation, J. Geophys. Res. Atmospheres, 114, https://doi.org/10.1029/2008JD011115, 2009.

Bhattacharjee, P. and Mitra, P.: A survey of density based clustering algorithms, Front. Comput. Sci., 15, 151308, https://doi.org/10.1007/s11704-019-9059-3, 2020.

Bohlmann, S., Shang, X., Giannakaki, E., Filioglou, M., Saarto, A., Romakkaniemi, S., and Komppula, M.: Detection and characterization of birch pollen in the atmosphere using a multiwavelength Raman polarization lidar and Hirst-type pollen sampler in Finland, Atmospheric Chem. Phys., 19, 14559–14569, https://doi.org/10.5194/acp-19-14559-2019, 2019.

Bohlmann, S., Shang, X., Vakkari, V., Giannakaki, E., Leskinen, A., Lehtinen, K. E. J., Pätsi, S., and Komppula, M.: Lidar depolarization ratio of atmospheric pollen at multiple wavelengths, Atmospheric Chem. Phys., 21, 7083–7097, https://doi.org/10.5194/acp-21-7083-2021, 2021.

Brunner, C., Brem, B. T., Collaud Coen, M., Conen, F., Hervo, M., Henne, S., Steinbacher, M., Gysel-Beer, M., and Kanji, Z. A.: The contribution of Saharan dust to the ice-nucleating particle concentrations at the High Altitude Station Jungfraujoch (3580 m a.s.l.), Switzerland, Atmospheric Chem. Phys., 21, 18029–18053, https://doi.org/10.5194/acp-21-18029-2021, 2021.

Brus, D., Gustafsson, J., Vakkari, V., Kemppinen, O., de Boer, G., and Hirsikko, A.: Measurement report: Properties of aerosol and gases in the vertical profile during the LAPSE-RATE campaign, Atmospheric Chem. Phys., 21, 517–533, https://doi.org/10.5194/acp-21-517-2021, 2021.

Burton, S. P., Ferrare, R. A., Hostetler, C. A., Hair, J. W., Rogers, R. R., Obland, M. D., Butler, C. F., Cook, A. L., Harper, D. B., and Froyd, K. D.: Aerosol classification using airborne High Spectral Resolution Lidar measurements – methodology and examples, Atmospheric Meas. Tech., 5, 73–98, https://doi.org/10.5194/amt-5-73-2012, 2012.

Burton, S. P., Hostetler, C. A., Cook, A. L., Hair, J. W., Seaman, S. T., Scola, S., Harper, D. B., Smith, J. A., Fenn, M. A., Ferrare, R. A., Saide, P. E., Chemyakin, E. V., and Müller, D.: Calibration of a high spectral resolution lidar using a Michelson interferometer, with data examples from ORACLES, Appl. Opt., 57, 6061–6075, https://doi.org/10.1364/AO.57.006061, 2018.

Chatziparaschos, M., Myriokefalitakis, S., Kalivitis, N., Daskalakis, N., Nenes, A., Gonçalves Ageitos, M., Costa-Surós, M., Pérez García-Pando, C., Vrekoussis, M., and Kanakidou, M.: Assessing the global contribution of marine aerosols, terrestrial bioaerosols, and desert dust to ice-nucleating particle concentrations, Atmospheric Chem. Phys., 25, 9085–9111, https://doi.org/10.5194/acp-25-9085-2025, 2025.

Chazette, P., Totems, J., and Shang, X.: Transport of aerosols over the French Riviera – link between ground-based lidar and spaceborne observations, Atmospheric Chem. Phys., 19, 3885–3904, https://doi.org/10.5194/acp-19-3885-2019, 2019.

Chen, J., Zeng, X., Li, S., Song, G., and Li, S.: Water Vapor Correction in Measurements of Aerosol Backscatter Coefficients Using a 910 nm Vaisala CL51 Ceilometer, Remote Sens., 17, 2013, https://doi.org/10.3390/rs17122013, 2025.

Cholleton, D., Rairoux, P., and Miffre, A.: Laboratory Evaluation of the (355, 532) nm Particle Depolarization Ratio of Pure Pollen at 180.0° Lidar Backscattering Angle, Remote Sens., 14, 3767, https://doi.org/10.3390/rs14153767, 2022.

Comerón, A., Muñoz-Porcar, C., Rocadenbosch, F., Rodríguez-Gómez, A., and Sicard, M.: Current Research in Lidar Technology Used for the Remote Sensing of Atmospheric Aerosols, Sensors, 17, 1450, https://doi.org/10.3390/s17061450, 2017.

Cuevas-Agulló, E., Barriopedro, D., García, R. D., Alonso-Pérez, S., González-Alemán, J. J., Werner, E., Suárez, D., Bustos, J. J., García-Castrillo, G., García, O., Barreto, Á., and Basart, S.: Sharp increase in Saharan dust intrusions over the western Euro-Mediterranean in February–March 2020–2022 and associated atmospheric circulation, Atmospheric Chem. Phys., 24, 4083–4104, https://doi.org/10.5194/acp-24-4083-2024, 2024.

Dall'Osto, M., Harrison, R. M., Highwood, E. J., O'Dowd, C., Ceburnis, D., Querol, X., and Achterberg, E. P.: Variation of the mixing state of Saharan dust particles with atmospheric transport, Atmos. Environ., 44, 3135–3146, https://doi.org/10.1016/j.atmosenv.2010.05.030, 2010.

Eskes, H., Tsikerdekis, A., Ades, M., Alexe, M., Benedictow, A. C., Bennouna, Y., Blake, L., Bouarar, I., Chabrillat, S., Engelen, R., Errera, Q., Flemming, J., Garrigues, S., Griesfeller, J., Huijnen, V., Ilić, L., Inness, A., Kapsomenakis, J., Kipling, Z., Langerock, B., Mortier, A., Parrington, M., Pison, I., Pitkänen, M., Remy, S., Richter, A., Schoenhardt, A., Schulz, M., Thouret, V., Warneke, T., Zerefos, C., and Peuch, V.-H.: Technical note: Evaluation of the Copernicus Atmosphere Monitoring Service Cy48R1 upgrade of June 2023, Atmospheric Chem. Phys., 24, 9475–9514, https://doi.org/10.5194/acp-24-9475-2024, 2024.

Ester, M., Kriegel, Hans-Peter, Sander, Jörg, and Xu, Xiaowei: A density-based algorithm for discovering clusters in large spatial databases with noise. Proc. 2nd Int. Conf. on Knowledge Discovery and Data Mining. Portland, OR, pp. 226–231., 1996.

Farhani, G., Sica, R. J., and Daley, M. J.: Classification of lidar measurements using supervised and unsupervised machine learning methods, Atmospheric Meas. Tech., 14, 391–402, https://doi.org/10.5194/amt-14-391-2021, 2021.

Ferrare, R., Hair, J., Hostetler, C., Shingler, T., Burton, S. P., Fenn, M., Clayton, M., Scarino, A. J., Harper, D., Seaman, S., Cook, A., Crosbie, E., Winstead, E., Ziemba, L., Thornhill, L., Robinson, C., Moore, R., Vaughan, M., Sorooshian, A., Schlosser, J. S., Liu, H., Zhang, B., Diskin, G., DiGangi, J., Nowak, J., Choi, Y., Zuidema, P., and Chellappan, S.: Airborne HSRL-2 measurements of elevated aerosol depolarization associated with non-spherical sea salt, Front. Remote Sens., 4, https://doi.org/10.3389/frsen.2023.1143944, 2023.

Filioglou, M., Leskinen, A., Vakkari, V., O'Connor, E., Tuononen, M., Tuominen, P., Laukkanen, S., Toiviainen, L., Saarto, A., Shang, X., Tiitta, P., and Komppula, M.: Spectral dependence of birch and pine pollen optical properties using a synergy of lidar instruments, Atmospheric Chem. Phys., 23, 9009–9021, https://doi.org/10.5194/acp-23-9009-2023, 2023.

Filioglou, M., Tiitta, P., Shang, X., Leskinen, A., Ahola, P., Pätsi, S., Saarto, A., Vakkari, V., Isopahkala, U., and Komppula, M.: Lidar estimates of birch pollen number, mass, and CCN-related concentrations, Atmospheric Chem. Phys., 25, 1639–1657, https://doi.org/10.5194/acp-25-1639-2025, 2025.

Flemish Environment Agency: Jaarrapport Lucht Emissies en concentraties van luchtverontreinigende stoffen [Core Writing Team, B. De Potter (ed.)]. VMM, Aalst, Belgium, pp. 1-180., 2020.

Flemming, J., Huijnen, V., Arteta, J., Bechtold, P., Beljaars, A., Blechschmidt, A.-M., Diamantakis, M., Engelen, R. J., Gaudel, A., Inness, A., Jones, L., Josse, B., Katragkou, E., Marecal, V., Peuch, V.-H., Richter, A., Schultz, M. G., Stein, O., and Tsikerdekis, A.: Tropospheric chemistry in the Integrated Forecasting System of ECMWF, Geosci. Model Dev., 8, 975–1003, https://doi.org/10.5194/gmd-8-975-2015, 2015.

https://doi.org/10.5194/egusphere-2026-948
Preprint. Discussion started: 21 April 2026

Flentje, H., Mattis, I., Kipling, Z., Rémy, S., and Thomas, W.: Evaluation of ECMWF IFS-AER (CAMS) operational forecasts during cycle 41r1–46r1 with calibrated ceilometer profiles over Germany, Geosci. Model Dev., 14, 1721–1751, https://doi.org/10.5194/gmd-14-1721-2021, 2021.

Franco, M. A., Valiati, R., Holanda, B. A., Meller, B. B., Kremper, L. A., Rizzo, L. V., Carbone, S., Morais, F. G., Nascimento, J. P., Andreae, M. O., Cecchini, M. A., Machado, L. A. T., Ponczek, M., Pöschl, U., Walter, D., Pöhlker, C., and Artaxo, P.: Vertically resolved aerosol variability at the Amazon Tall Tower Observatory under wet-season conditions, Atmospheric Chem. Phys., 24, 8751–8770, https://doi.org/10.5194/acp-24-8751-2024, 2024.

Freney, E. J., Sellegri, K., Canonaco, F., Boulon, J., Hervo, M., Weigel, R., Pichon, J. M., Colomb, A., Prévôt, A. S. H., and Laj, P.: Seasonal variations in aerosol particle composition at the puy-de-Dôme research station in France, Atmospheric Chem. Phys., 11, 13047–13059, https://doi.org/10.5194/acp-11-13047-2011, 2011.

Freudenthaler, V., Esselborn, M., Wiegner, M., Heese, B., Tesche, M., Ansmann, A., Müller, D., Althausen, D., Wirth, M., Fix, A., Ehret, G., Knippertz, P., Toledano, C., Gasteiger, J., Garhammer, M., and Seefeldner, M.: Depolarization ratio profiling at several wavelengths in pure Saharan dust during SAMUM 2006, Tellus B, 61, 165–179, https://doi.org/10.1111/j.1600-0889.2008.00396.x, 2009.

Groß, S., Freudenthaler, V., Wiegner, M., Gasteiger, J., Geiß, A., and Schnell, F.: Dual-wavelength linear depolarization ratio of volcanic aerosols: Lidar measurements of the Eyjafjallajökull plume over Maisach, Germany, Atmos. Environ., 48, 85–96, https://doi.org/10.1016/j.atmosenv.2011.06.017, 2012.

Groß, S., Esselborn, M., Weinzierl, B., Wirth, M., Fix, A., and Petzold, A.: Aerosol classification by airborne high spectral resolution lidar observations, Atmospheric Chem. Phys., 13, 2487–2505, https://doi.org/10.5194/acp-13-2487-2013, 2013.

Haarig, M., Ansmann, A., Gasteiger, J., Kandler, K., Althausen, D., Baars, H., Radenz, M., and Farrell, D. A.: Dry versus wet marine particle optical properties: RH dependence of depolarization ratio, backscatter, and extinction from multiwavelength lidar measurements during SALTRACE, Atmospheric Chem. Phys., 17, 14199–14217, https://doi.org/10.5194/acp-17-14199-2017, 2017.

Hair, J. W., Hostetler, C. A., Cook, A. L., Harper, D. B., Ferrare, R. A., Mack, T. L., Welch, W., Izquierdo, L. R., and Hovis, F. E.: Airborne High Spectral Resolution Lidar for profiling aerosol optical properties, Appl. Opt., 47, 6734–6752, https://doi.org/10.1364/AO.47.006734, 2008.

Harvey, N. J., Hogan, R. J., and Dacre, H. F.: A method to diagnose boundary-layer type using Doppler lidar, Q. J. R. Meteorol. Soc., 139, 1681–1693, https://doi.org/10.1002/qj.2068, 2013.

https://doi.org/10.5194/egusphere-2026-948
Preprint. Discussion started: 21 April 2026

Hoebeke, L., Bruffaerts, N., Verstraeten, C., Delcloo, A., De Smedt, T., Packeu, A., Detandt, M., and Hendrickx, M.: Thirty-four years of pollen monitoring: an evaluation of the temporal variation of pollen seasons in Belgium, Aerobiologia, 34, 139–155, https://doi.org/10.1007/s10453-017-9503-5, 2018.

Hopkin, E., Illingworth, A. J., Charlton-Perez, C., Westbrook, C. D., and Ballard, S.: A robust automated technique for operational calibration of ceilometers using the integrated backscatter from totally attenuating liquid clouds, Atmospheric Meas. Tech., 12, 4131–4147, https://doi.org/10.5194/amt-12-4131-2019, 2019.

Hu, Q., Goloub, P., Veselovskii, I., Bravo-Aranda, J.-A., Popovici, I. E., Podvin, T., Haeffelin, M., Lopatin, A., Dubovik, O., Pietras, C., Huang, X., Torres, B., and Chen, C.: Long-range-transported Canadian smoke plumes in the lower stratosphere over northern France, Atmospheric Chem. Phys., 19, 1173–1193, https://doi.org/10.5194/acp-19-1173-2019, 2019.

Hu, Y., Liu, Z., Winker, D., Vaughan, M., Noel, V., Bissonnette, L., Roy, G., and McGill, M.: Simple relation between lidar multiple scattering and depolarization for water clouds, Opt. Lett., 31, 1809–1811, https://doi.org/10.1364/ol.31.001809, 2006.

Huneeus, N., Schulz, M., Balkanski, Y., Griesfeller, J., Prospero, J., Kinne, S., Bauer, S., Boucher, O., Chin, M., Dentener, F., Diehl, T., Easter, R., Fillmore, D., Ghan, S., Ginoux, P., Grini, A., Horowitz, L., Koch, D., Krol, M. C., Landing, W., Liu, X., Mahowald, N., Miller, R., Morcrette, J.-J., Myhre, G., Penner, J., Perlwitz, J., Stier, P., Takemura, T., and Zender, C. S.: Global dust model intercomparison in AeroCom phase I, Atmospheric Chem. Phys., 11, 7781–7816, https://doi.org/10.5194/acp-11-7781-2011, 2011.

Illingworth, A. J., Hogan, R. J., O’Connor, E. J., Bouniol, D., Brooks, M. E., Delanoé, J., Donovan, D. P., Eastment, J. D., Gaussiat, N., Goddard, J. W. F., Haeffelin, M., Baltink, H. K., Krasnov, O. A., Pelon, J., Piriou, J.-M., Protat, A., Russchenberg, H. W. J., Seifert, A., Tompkins, A. M., Zadelhoff, G.-J. van, Vinit, F., Willén, U., Wilson, D. R., and Wrench, C. L.: Cloudnet: Continuous Evaluation of Cloud Profiles in Seven Operational Models Using Ground-Based Observations, Bull. Am. Meteorol. Soc., 88, 883–898, https://doi.org/10.1175/BAMS-88-6-883, 2007.

Illingworth, A. J., Barker, H. W., Beljaars, A., Ceccaldi, M., Chepfer, H., Clerbaux, N., Cole, J., Delanoë, J., Domenech, C., Donovan, D. P., Fukuda, S., Hirakata, M., Hogan, R. J., Huenerbein, A., Kollias, P., Kubota, T., Nakajima, T., Nakajima, T. Y., Nishizawa, T., Ohno, Y., Okamoto, H., Oki, R., Sato, K., Satoh, M., Shephard, M. W., Velázquez-Blázquez, A., Wandinger, U., Wehr, T., and Zadelhoff, G.-J. van: The EarthCARE Satellite: The Next Step Forward in Global Measurements of Clouds, Aerosols, Precipitation, and Radiation, Bull. Am. Meteorol. Soc., 96, 1311–1332, https://doi.org/10.1175/BAMS-D-12-00227.1, 2015.

Illingworth, A. J., Cimini, D., Haefele, A., Haeffelin, M., Hervo, M., Kotthaus, S., Löhnert, U., Martinet, P., Mattis, I., O’Connor, E. J., and Potthast, R.: How Can Existing Ground-Based Profiling Instruments Improve European Weather Forecasts?, Bull. Am. Meteorol. Soc., 100, 605–619, https://doi.org/10.1175/BAMS-D-17-0231.1, 2019.

Inoue, J. and Sato, K.: Comparison of the depolarization measurement capability of a lidar ceilometer with cloud particle sensor sondes: A case study of liquid water clouds, Polar Sci., 35, 100911, https://doi.org/10.1016/j.polar.2022.100911, 2023.

Inoue, J., Sato, K., and Shimizu, S.: Shipboard observational evidence of supercooled liquid water clouds in the mid-troposphere over the Southern Ocean, Sci. Rep., 15, 18617, https://doi.org/10.1038/s41598-025-03119-z, 2025.

Ionita, M. and Nagavciuc, V.: 2024: The year with too much summer in the eastern part of Europe, Weather, 80, 288–295, https://doi.org/10.1002/wea.7696, 2025.

Ionita, M., Vaideanu, P., Nichita, D., and Nagavciuc, V.: Breaking records under clear skies: the impact of sunshine duration and atmospheric dynamics on the 2024 Eastern European extreme summer temperatures, Npj Nat. Hazards, 2, 82, https://doi.org/10.1038/s44304-025-00137-9, 2025.

IPCC: Climate Change 2023: Synthesis Report. Contribution of Working Groups I, II and III to the Sixth Assessment Report of the Intergovernmental Panel on Climate Change [Core Writing Team, H. Lee and J. Romero (eds.)]. IPCC, Geneva, Switzerland, pp. 35-115., https://doi.org/10.59327/IPCC/AR6-9789291691647, 2023.

IRCELINE: RAPPORT ANNUEL 2023 de la qualité de l’air en Belgique. IRCELINE, Brussels, Belgium, pp. 1-64., 2023.

Jurányi, Z., Lüpkes, C., Stratmann, F., Hartmann, J., Schaefer, J., Jörss, A.-M., Schulz, A., Wetzel, B., Simon, D., Gebhard, E., Stöhr, M., Hofmann, P., Kalmbach, D., Grawe, S., Wendisch, M., and Herber, A.: The T-Bird – a new aircraft-towed instrument platform to measure aerosol properties and turbulence close to the surface: introduction to the aerosol measurement system, Atmospheric Meas. Tech., 18, 3477–3494, https://doi.org/10.5194/amt-18-3477-2025, 2025.

Karle, N. N., Sakai, R. K., Fitzgerald, R. M., Ichoku, C., Mercado, F., and Stockwell, W. R.: Systematic analysis of virga and its impact on surface particulate matter observations, Atmospheric Meas. Tech., 16, 1073–1085, https://doi.org/10.5194/amt-16-1073-2023, 2023.

Karle, N. N., Sakai, R. K., Rossi, R. D., Flores, A., and Chiao, S.: Vertical profiling of Canadian wildfire smoke in the Baltimore-Washington Corridor – interactions with the planetary boundary layer and impact on surface air quality, Atmospheric Meas. Tech., 18, 6727–6746, https://doi.org/10.5194/amt-18-6727-2025, 2025.

Klingebiel, M., Ghate, V. P., Naumann, A. K., Ditas, F., Pöhlker, M. L., Pöhlker, C., Kandler, K., Konow, H., and Stevens, B.: Remote Sensing of Sea Salt Aerosol below Trade Wind Clouds, J. Atmospheric Sci., 76, 1189–1202, https://doi.org/10.1175/JAS-D-18-0139.1, 2019.

Le, V., Lobo, H., O'Connor, E. J., and Vakkari, V.: Long-term aerosol particle depolarization ratio measurements with HALO Photonics Doppler lidar, Atmospheric Meas. Tech., 17, 921–941, https://doi.org/10.5194/amt-17-921-2024, 2024.

Lewis, J. R., Campbell, J. R., Stewart, S. A., Tan, I., Welton, E. J., and Lolli, S.: Determining cloud thermodynamic phase from the polarized Micro Pulse Lidar, Atmospheric Meas. Tech., 13, 6901–6913, https://doi.org/10.5194/amt-13-6901-2020, 2020.

Liou, K.-N. and Schotland, R. M.: Multiple Backscattering and Depolarization from Water Clouds for a Pulsed Lidar System, J. Atmospheric Sci., 28, 772–784, https://doi.org/10.1175/1520-0469(1971)028%253C0772:MBADFW%253E2.0.CO;2, 1971.

Lolli, S.: Machine Learning Techniques for Vertical Lidar-Based Detection, Characterization, and Classification of Aerosols and Clouds: A Comprehensive Survey, Remote Sens., 15, 4318, https://doi.org/10.3390/rs15174318, 2023.

Looschelders, D., Christen, A., Grimmond, S., Kotthaus, S., Fenner, D., Dupont, J.-C., Haeffelin, M., and Morrison, W.: Inter-Instrument Variability of Vaisala CL61 Lidar-Ceilometer's Attenuated Backscatter, Cloud Properties and Mixed-Layer Height, Meteorol. Appl., 32, e70088, https://doi.org/10.1002/met.70088, 2025.

Madonna, F., Amato, F., Vande Hey, J., and Pappalardo, G.: Ceilometer aerosol profiling versus Raman lidar in the frame of the INTERACT campaign of ACTRIS, Atmospheric Meas. Tech., 8, 2207–2223, https://doi.org/10.5194/amt-8-2207-2015, 2015.

Madonna, F., Rosoldi, M., Lolli, S., Amato, F., Vande Hey, J., Dhillon, R., Zheng, Y., Brettle, M., and Pappalardo, G.: Intercomparison of aerosol measurements performed with multi-wavelength Raman lidars, automatic lidars and ceilometers in the framework of INTERACT-II campaign, Atmospheric Meas. Tech., 11, 2459–2475, https://doi.org/10.5194/amt-11-2459-2018, 2018.

Manninen, A. J., Marke, T., Tuononen, M., and O'Connor, E. J.: Atmospheric Boundary Layer Classification With Doppler Lidar, J. Geophys. Res. Atmospheres, 123, 8172–8189, https://doi.org/10.1029/2017JD028169, 2018.

Marinou, E., Amiridis, V., Binietoglou, I., Tsikerdekis, A., Solomos, S., Proestakis, E., Konsta, D., Papagiannopoulos, N., Tsekeri, A., Vlastou, G., Zanis, P., Balis, D., Wandinger, U., and Ansmann, A.: Three-dimensional evolution of Saharan dust transport towards Europe based on a 9-year EARLINET-optimized CALIPSO dataset, Atmospheric Chem. Phys., 17, 5893–5919, https://doi.org/10.5194/acp-17-5893-2017, 2017.

Markowicz, K. M., Pakszys, P., Ritter, C., Zielinski, T., Udisti, R., Cappelletti, D., Mazzola, M., Shiobara, M., Xian, P., Zawadzka, O., Lisok, J., Petelski, T., Makuch, P., and Karasiński, G.: Impact of North American intense fires on aerosol optical properties measured over the European Arctic in July 2015, J. Geophys. Res. Atmospheres, 121, 14,487-14,512, https://doi.org/10.1002/2016JD025310, 2016.

Masoom, A., Kazadzis, S., Modini, R. L., Gysel-Beer, M., Gröbner, J., Coen, M. C., Navas-Guzman, F., Kouremeti, N., Brem, B. T., Nowak, N. K., Martucci, G., Hervo, M., and Erb, S.: Long range transport of Canadian Wildfire smoke to Europe in Fall 2023: aerosol properties and spectral features of smoke particles, EGUsphere, 1–43, https://doi.org/10.5194/egusphere-2025-2755, 2025.

Mattis, I., Müller, D., Ansmann, A., Wandinger, U., Preißler, J., Seifert, P., and Tesche, M.: Ten years of multiwavelength Raman lidar observations of free-tropospheric aerosol layers over central Europe: Geometrical properties and annual cycle, J. Geophys. Res. Atmospheres, 113, https://doi.org/10.1029/2007JD009636, 2008.

Monteiro, A., Basart, S., Kazadzis, S., Votsis, A., Gkikas, A., Vandenbussche, S., Tobias, A., Gama, C., García-Pando, C. P., Terradellas, E., Notas, G., Middleton, N., Kushta, J., Amiridis, V., Lagouvardos, K., Kosmopoulos, P., Kotroni, V., Kanakidou, M., Mihalopoulos, N., Kalivitis, N., Dagsson-Waldhauserová, P., El-Askary, H., Sievers, K., Giannaros, T., Mona, L., Hirtl, M., Skomorowski, P., Virtanen, T. H., Christoudias, T., Di Mauro, B., Trippetta, S., Kutuzov, S., Meinander, O., and Nickovic, S.: Multi-sectoral impact assessment of an extreme African dust episode in the Eastern Mediterranean in March 2018, Sci. Total Environ., 843, 156861, https://doi.org/10.1016/j.scitotenv.2022.156861, 2022.

Morcrette, J.-J., Boucher, O., Jones, L., Salmond, D., Bechtold, P., Beljaars, A., Benedetti, A., Bonet, A., Kaiser, J. W., Razinger, M., Schulz, M., Serrar, S., Simmons, A. J., Sofiev, M., Suttie, M., Tompkins, A. M., and Untch, A.: Aerosol analysis and forecast in the European Centre for Medium-Range Weather Forecasts Integrated Forecast System: Forward modeling, J. Geophys. Res. Atmospheres, 114, https://doi.org/10.1029/2008JD011235, 2009.

Morille, Y., Haeffelin, M., Drobinski, P., and Pelon, J.: STRAT: An Automated Algorithm to Retrieve the Vertical Structure of the Atmosphere from Single-Channel Lidar Data, J. Atmospheric Ocean. Technol., 24, 761–775, https://doi.org/10.1175/JTECH2008.1, 2007.

Müller, D., Ansmann, A., Mattis, I., Tesche, M., Wandinger, U., Althausen, D., and Pisani, G.: Aerosol-type-dependent lidar ratios observed with Raman lidar, J. Geophys. Res. Atmospheres, 112, https://doi.org/10.1029/2006JD008292, 2007.

Neely, R. R., Hayman, M., Stillwell, R., Thayer, J. P., Hardesty, R. M., O'Neill, M., Shupe, M. D., and Alvarez, C.: Polarization Lidar at Summit, Greenland, for the Detection of Cloud Phase and Particle Orientation, J. Atmospheric Ocean. Technol., 30, 1635–1655, https://doi.org/10.1175/JTECH-D-12-00101.1, 2013.

Nicolae, D., Vasilescu, J., Talianu, C., Binietoglou, I., Nicolae, V., Andrei, S., and Antonescu, B.: A neural network aerosol-typing algorithm based on lidar data, Atmospheric Chem. Phys., 18, 14511–14537, https://doi.org/10.5194/acp-18-14511-2018, 2018.

Noh, Y. M., Lee, H., Mueller, D., Lee, K., Shin, D., Shin, S., Choi, T. J., Choi, Y. J., and Kim, K. R.: Investigation of the diurnal pattern of the vertical distribution of pollen in the lower troposphere using LIDAR, Atmospheric Chem. Phys., 13, 7619–7629, https://doi.org/10.5194/acp-13-7619-2013, 2013.

O'Connor, E. J., Illingworth, A. J., and Hogan, R. J.: A Technique for Autocalibration of Cloud Lidar, J. Atmospheric Ocean. Technol., 21, 777–786, https://doi.org/10.1175/1520-0426(2004)021%253C0777:ATFAOC%253E2.0.CO;2, 2004.

O'Connor, E. J., Hogan, R. J., and Illingworth, A. J.: Retrieving Stratocumulus Drizzle Parameters Using Doppler Radar and Lidar, J. Appl. Meteorol. Climatol., 44, 14–27, https://doi.org/10.1175/JAM-2181.1, 2005.

Papayannis, A., Amiridis, V., Mona, L., Tsaknakis, G., Balis, D., Bösenberg, J., Chaikovski, A., De Tomasi, F., Grigorov, I., Mattis, I., Mitev, V., Müller, D., Nickovic, S., Pérez, C., Pietruczuk, A., Pisani, G., Ravetta, F., Rizi, V., Sicard, M., Trickl, T., Wiegner, M., Gerding, M., Mamouri, R. E., D'Amico, G., and Pappalardo, G.: Systematic lidar observations of Saharan dust over Europe in the frame of EARLINET (2000–2002), J. Geophys. Res. Atmospheres, 113, https://doi.org/10.1029/2007JD009028, 2008.

Papetta, A., Marenco, F., Kezoudi, M., Mamouri, R.-E., Nisantzi, A., Baars, H., Popovici, I. E., Goloub, P., Victori, S., and Sciare, J.: Lidar depolarization characterization using a reference system, Atmospheric Meas. Tech., 17, 1721–1738, https://doi.org/10.5194/amt-17-1721-2024, 2024.

Petäjä, T., Laakso, L., Grönholm, T., Launiainen, S., Evele-Peltoniemi, I., Virkkula, A., Leskinen, A., Backman, J., Manninen, H. E., Sipilä, M., Haapanala, S., Hämeri, K., Vanhala, E., Tuomi, T., Paatero, J., Aurela, M., Hakola, H., Makkonen, U., Hellén, H., Hillamo, R., Vira, J., Prank, M., Sofiev, M., Siitari-Kauppi, M., Laaksonen, A., lehtinen, K. E. J., Kulmala, M., Viisanen, Y., and Kerminen, V.-M.: In-situ observations of Eyjafjallajökull ash particles by hot-air balloon, Atmos. Environ., 48, 104–112, https://doi.org/10.1016/j.atmosenv.2011.08.046, 2012.

Peuch, V.-H., Engelen, R., Rixen, M., Dee, D., Flemming, J., Suttie, M., Ades, M., Agustí-Panareda, A., Ananasso, C., Andersson, E., Armstrong, D., Barré, J., Bousserez, N., Dominguez, J. J., Garrigues, S., Inness, A., Jones, L., Kipling, Z., Letertre-Danczak, J., Parrington, M., Razinger, M., Ribas, R., Vermoote, S., Yang, X., Simmons, A., Marcilla, J. G. de, and Thépaut, J.-N.: The Copernicus Atmosphere Monitoring Service: From Research to Operations, Bull. Am. Meteorol. Soc., 103, E2650–E2668, https://doi.org/10.1175/BAMS-D-21-0314.1, 2022.

Pio, C. A., Legrand, M., Oliveira, T., Afonso, J., Santos, C., Caseiro, A., Fialho, P., Barata, F., Puxbaum, H., Sanchez-Ochoa, A., Kasper-Giebl, A., Gelencsér, A., Preunkert, S., and Schock, M.: Climatology of aerosol composition (organic versus inorganic) at nonurban sites on a west-east transect across Europe, J. Geophys. Res. Atmospheres, 112, https://doi.org/10.1029/2006JD008038, 2007.

Putaud, J.-P., Van Dingenen, R., Alastuey, A., Bauer, H., Birmili, W., Cyrys, J., Flentje, H., Fuzzi, S., Gehrig, R., Hansson, H. C., Harrison, R. M., Herrmann, H., Hitzenberger, R., Hüglin, C., Jones, A. M., Kasper-Giebl, A., Kiss, G., Kousa, A., Kuhlbusch, T. A. J., Löschau, G., Maenhaut, W., Molnar, A., Moreno, T., Pekkanen, J., Perrino, C., Pitz, M., Puxbaum, H., Querol, X., Rodriguez, S., Salma, I., Schwarz, J., Smolik, J., Schneider, J., Spindler, G., ten Brink, H., Tursic, J., Viana, M., Wiedensohler, A., and Raes, F.: A European aerosol phenomenology – 3: Physical and chemical characteristics of particulate matter from 60 rural, urban, and kerbside sites across Europe, Atmos. Environ., 44, 1308–1320, https://doi.org/10.1016/j.atmosenv.2009.12.011, 2010.

Ravi Kiran, V., Venkat Ratnam, M., Fujiwara, M., Russchenberg, H., Wienhold, F. G., Madhavan, B. L., Roja Raman, M., Nandan, R., Akhil Raj, S. T., Hemanth Kumar, A., and Ravindra Babu, S.: Balloon-borne aerosol–cloud interaction studies (BACIS): field campaigns to understand and quantify aerosol effects on clouds, Atmospheric Meas. Tech., 15, 4709–4734, https://doi.org/10.5194/amt-15-4709-2022, 2022.

Reid, J. S., Koppmann, R., Eck, T. F., and Eleuterio, D. P.: A review of biomass burning emissions part II: intensive physical properties of biomass burning particles, Atmospheric Chem. Phys., 5, 799–825, https://doi.org/10.5194/acp-5-799-2005, 2005.

Rémy, S., Kipling, Z., Flemming, J., Boucher, O., Nabat, P., Michou, M., Bozzo, A., Ades, M., Huijnen, V., Benedetti, A., Engelen, R., Peuch, V.-H., and Morcrette, J.-J.: Description and evaluation of the tropospheric aerosol scheme in the European Centre for Medium-Range Weather Forecasts (ECMWF) Integrated Forecasting System (IFS-AER, cycle 45R1), Geosci. Model Dev., 12, 4627–4659, https://doi.org/10.5194/gmd-12-4627-2019, 2019.

Roininen, R., Tuononen, M., Bircher-Adrot, S., Rüfenacht, R., O'Connor, E., Buxmann, J., Kotthaus, S., Van Hove, M., Diémoz, H., BELLINI, A., Fenner, D., Looschelders, D., Geiß, A., Wagner, F., and Mattis, I.: SOP CL61, Zenodo, https://doi.org/10.5281/zenodo.14833761, 2025.

Schepanski, K., Tegen, I., and Macke, A.: Saharan dust transport and deposition towards the tropical northern Atlantic, Atmospheric Chem. Phys., 9, 1173–1189, https://doi.org/10.5194/acp-9-1173-2009, 2009.

Seinfeld, J. H. and Pandis, S. N.: Atmospheric Chemistry and Physics: From Air Pollution to Climate Change, Wiley, 1366 pp., 1998.

Sicard, M., Izquierdo, R., Alarcón, M., Belmonte, J., Comerón, A., and Baldasano, J. M.: Near-surface and columnar measurements with a micro pulse lidar of atmospheric pollen in Barcelona, Spain, Atmospheric Chem. Phys., 16, 6805–6821, https://doi.org/10.5194/acp-16-6805-2016, 2016.

Sicard, M., Granados-Muñoz, M. J., Alados-Arboledas, L., Barragán, R., Bedoya-Velásquez, A. E., Benavent-Oltra, J. A., Bortoli, D., Comerón, A., Córdoba-Jabonero, C., Costa, M. J., del Águila, A., Fernández, A. J., Guerrero-Rascado, J. L., Jorba, O., Molero, F., Muñoz-Porcar, C., Ortiz-Amezcua, P., Papagiannopoulos, N., Potes, M., Pujadas, M., Rocadenbosch, F., Rodríguez-Gómez, A., Román, R., Salgado, R., Salgueiro, V., Sola, Y., and Yela, M.: Ground/space, passive/active remote sensing observations coupled with particle dispersion modelling to understand the inter-continental transport of wildfire smoke plumes, Remote Sens. Environ., 232, 111294, https://doi.org/10.1016/j.rse.2019.111294, 2019.

Souri, A. H., Choi, Y., Jeon, W., Kochanski, A. K., Diao, L., Mandel, J., Bhave, P. V., and Pan, S.: Quantifying the Impact of Biomass Burning Emissions on Major Inorganic Aerosols and Their Precursors in the U.S., J. Geophys. Res. Atmospheres, 122, 12,020-12,041, https://doi.org/10.1002/2017JD026788, 2017.

Tillmann, R., Gkatzelis, G. I., Rohrer, F., Winter, B., Wesolek, C., Schuldt, T., Lange, A. C., Franke, P., Friese, E., Decker, M., Wegener, R., Hundt, M., Aseev, O., and Kiendler-Scharr, A.: Air quality observations onboard commercial and targeted Zeppelin flights in Germany – a platform for high-resolution trace-gas and aerosol measurements within the planetary boundary layer, Atmospheric Meas. Tech., 15, 3827–3842, https://doi.org/10.5194/amt-15-3827-2022, 2022.

Tukiainen, S., Siipola, T., Leskinen, N., and O’Connor, E.: Remote sensing measurements during PaCE 2022 campaign, Earth Syst. Sci. Data, 17, 3797–3806, https://doi.org/10.5194/essd-17-3797-2025, 2025.

VAISALA: White Paper, Vaisala Lidar Ceilometer CL61, Depolarization measurement with ceilometer. VAISALA, Helsinki, Finland,pp 2-3. https://www.vaisala.com/sites/default/files/documents/WEA-MET-WhitePaper-CL61-B212267EN-A.pdf, 2021.

Vakkari, V., Baars, H., Bohlmann, S., Bühl, J., Komppula, M., Mamouri, R.-E., and O’Connor, E. J.: Aerosol particle depolarization ratio at 1565 nm measured with a Halo Doppler lidar, Atmospheric Chem. Phys., 21, 5807–5820, https://doi.org/10.5194/acp-21-5807-2021, 2021.

Van Tricht, K., Gorodetskaya, I. V., Lhermitte, S., Turner, D. D., Schween, J. H., and Van Lipzig, N. P. M.: An improved algorithm for polar cloud-base detection by ceilometer over the ice sheets, Atmospheric Meas. Tech., 7, 1153–1167, https://doi.org/10.5194/amt-7-1153-2014, 2014.

Varutbangkul, V., Brechtel, F. J., Bahreini, R., Ng, N. L., Keywood, M. D., Kroll, J. H., Flagan, R. C., Seinfeld, J. H., Lee, A., and Goldstein, A. H.: Hygroscopicity of secondary organic aerosols formed by oxidation of cycloalkenes, monoterpenes, sesquiterpenes, and related compounds, Atmospheric Chem. Phys., 6, 2367–2388, https://doi.org/10.5194/acp-6-2367-2006, 2006.

Verstraeten, W. W., Kouznetsov, R., Bruffaerts, N., Sofiev, M., and Delcloo, A. W.: Analyzing the airborne birch and grass pollen monitoring network of Belgium, Aerobiologia, 41, 211–227, https://doi.org/10.1007/s10453-025-09846-0, 2025.

Vogel, F., Putero, D., Bonasoni, P., Cristofanelli, P., Zanatta, M., and Marinoni, A.: Saharan dust transport event characterization in the Mediterranean atmosphere using 21 years of in-situ observations, Atmospheric Chem. Phys., 25, 15453–15468, https://doi.org/10.5194/acp-25-15453-2025, 2025.

https://doi.org/10.5194/egusphere-2026-948
Preprint. Discussion started: 21 April 2026

Wagner, F., Geiss, A., Barnaba, F., Belegante, L., Bellini, A., Buxmann, J., Diémoz, H., Fenner, D., Kotthaus, S., Osborne, M., Ruefenacht, R., Ruiz de Morales Céspedes, J., and Van Hove, M.: JND European networks observing the atmospheric boundary layer: Overview, access and impacts - Chapter 2a: Automatic low-power Lidar and Ceilometer (ALC), Zenodo, https://doi.org/10.5281/zenodo.11211873, 2024.

de Weger, L. A., Bruffaerts, N., Koenders, M. M. J. F., Verstraeten, W. W., Delcloo, A. W., Hentges, P., and Hentges, F.: Long-Term Pollen Monitoring in the Benelux: Evaluation of Allergenic Pollen Levels and Temporal Variations of Pollen Seasons, Front. Allergy, 2, https://doi.org/10.3389/falgy.2021.676176, 2021.

Wehr, T., Kubota, T., Tzeremes, G., Wallace, K., Nakatsuka, H., Ohno, Y., Koopman, R., Rusli, S., Kikuchi, M., Eisinger, M., Tanaka, T., Taga, M., Deghaye, P., Tomita, E., and Bernaerts, D.: The EarthCARE mission – science and system overview, Atmospheric Meas. Tech., 16, 3581–3608, https://doi.org/10.5194/amt-16-3581-2023, 2023.

Wiegner, M., Madonna, F., Binietoglou, I., Forkel, R., Gasteiger, J., Geiß, A., Pappalardo, G., Schäfer, K., and Thomas, W.: What is the benefit of ceilometers for aerosol remote sensing? An answer from EARLINET, Atmospheric Meas. Tech., 7, 1979–1997, https://doi.org/10.5194/amt-7-1979-2014, 2014.

Winker, D. M., Vaughan, M. A., Omar, A., Hu, Y., Powell, K. A., Liu, Z., Hunt, W. H., and Young, S. A.: Overview of the CALIPSO Mission and CALIOP Data Processing Algorithms, J. Atmospheric Ocean. Technol., 26, 2310–2323, https://doi.org/10.1175/2009JTECHA1281.1, 2009.

Zender, C. S., Bian, H., and Newman, D.: Mineral Dust Entrainment and Deposition (DEAD) model: Description and 1990s dust climatology, J. Geophys. Res. Atmospheres, 108, https://doi.org/10.1029/2002JD002775, 2003.